UNIVERSITY OF OKLAHOMA

GRADUATE COLLEGE

Three-Dimensional Anti-Jamming Array Processing for GNSS-Based Navigational Aid Inspection

A THESIS

SUBMITTED TO THE GRADUATE FACULTY

in partial fulfillment of the requirements for the

Degree of

MASTER OF SCIENCE

By

Olivia Hope Wolfley
Norman, Oklahoma
2023

Three-Dimensional Anti-Jamming Array Processing
for GNSS-Based Navigational Aid Inspection

A THESIS APPROVED FOR THE
SCHOOL OF ELECTRICAL AND COMPUTER ENGINEERING

BY THE COMMITTEE CONSISTING OF

Dr. Yan Zhang, Chair

Dr. David Schvartzman

Dr. Hernan Suarez

Acknowledgments

I struggle to describe the amount of gratitude I have for the people I am about to mention. I continue to be surprised by the kindness I come across in the OU ECE department from students and faculty. The people that I have met at OU have made my time here a very joyous experience. To my advisor, Dr. Rockee Zhang, thank you for always being available for questions and thank you for having a "can-do" attitude and a positive outlook. Thank you for leading me - I have really enjoyed working under you. To Dr. David Schvartzman, you have answered many, many questions of mine and you have done so with patience and in-depth answers which I am very grateful for. Thank you for sharing so much of your time and knowledge with me. To Dr. Hernan Suarez, thank you for being kind and willing to help me. In no special order, thank you to the following people who really helped me in different ways - Dr. Chad Davis, Dale Sexton, Khuda Burdi, Elizabeth Joyce, Jakob Fusselman, Brandon Mansur, Marcelo Marin, Luis Felipe Moncada Calmet, Rachael Cross, Dr. Jorge Salazar, Dr. Stephen Bass, Alexis Oblitas Mantilla, Dwight Caras, Stephanie Gill, Robert Rucker, Dr. Hjalti Sigmarsson, Dr. Justin Metcalf, and Michael Asante. To my family, you people are crazy but you are my favorite people and I don't deserve you all. Thanks to Jesus Christ, my rescuer.

Contents

List Of Tables

List Of Figures

Abstract

Global Navigational Satellite System (GNSS) Radio Frequency (RF) links are susceptible to interference. In signal compromised environments, the capability to combat RF interference (such as jamming) is necessary. Techniques and results of applying adaptive anti-jamming beam/null-forming processing to the measured three-dimensional (3D) and two-dimensional (2D) radiation patterns of L1-Band RHCP GNSS antenna arrays are investigated. Also, for reference studies in this thesis and for verification of null-forming methods, an S-Band antenna array is investigated. I developed a small-scale 2 by 3 and 1 by 6 custom arrays along with a 7-element circular array for demonstrating the GPS L1-Band operation. For the S-Band, a pre-built 1 by 8 linear array was used.

The visualization of the GPS array pattern through synthesis and direct measurements serves as the basis for algorithm implementations. Individual antenna element measurements are collected first and then, in post-processing, nulling techniques are applied. A digital beamformer generates weighted vectors for each element based on the locations of the multiple interfering signals. The covariance matrix of the interfering signals is utilized. Its inverse is taken and multiplied by the steering vector of the desired signal.

The goal is to optimize the locations and depths of the nulls to suppress the unwanted interference while still having the main beam directed toward the desired signal. Generated beam-forming coefficients are applied through digital post-processing and through an analog phased array controller. The digital and analog methods are

compared against each other. The evaluation of these null-forming techniques and measurement processes will be beneficial for the analysis of both civilian and military GNSS-based landing and navigational support systems.

Chapter 1

Introduction

1.1 Preface

Adaptive null-forming and three-dimensional digital beamforming (3D-DBF) are useful technologies in both wireless communication and radar. This work focuses on the application of adaptive null-forming and 3D-DBF for the Global Navigation Satellite System (GNSS) analysis and calibration. One of the key threats to GNSS operations is the interference, or jamming, from surrounding airspace, especially in battlefields. The challenge is to use small planar and linear arrays to create optimal nulls in 2D directions with two degrees of freedom. These nulls are regions in the radiation pattern where the signal-to-interference and noise ratio (SINR) are maximized to block interfering signals. There are many existing research documents on the anti-jamming GNSS antennas in Maloney (2020), Brachvogel et al. (2020) and Kraus (2014). However, studies lack systematic approach for three-dimensional pattern verification, and most of them are not well-calibrated for flight inspection mission. In this work, small-scale, passive GNSS receive antenna arrays are designed using commercial off-the-shelf GNSS receive elements. The antenna arrays lay on a ground plane and are placed in both far-field (FF) and near-field (NF) anechoic chambers. By controlling the positioner's orientation, we measure the 3D radiation pattern of each array element and record their data individually before combining the data in post-processing. A

3D visualization of these measured patterns is created and is then used for the initial application of the DBF algorithms. The processing algorithm has multiple iterations to generate various locations of nulls which correspond to various directions of incoming interference signals. Different 3D-DBF algorithms (as extensions of linear array DBF algorithms) can be applied to the measured element pattern data, and the anti-jamming performance will be evaluated based on the post-synthesized array patterns over broad azimuth and elevation angles. This work is beneficial to the future characterization and design of navigational aid antennas as well as the analysis of both civilian and military flight operations and applications

1.2 Challenges of GPS Signal Reception

GPS signals travel around 20,000 kilometers from their satellite's orbital path to the transmit/receive (TX/RX) antenna on an aircraft or ground location. When GPS antennas receive signals from these navigational satellites, the signal power is very low due to the travel distance. This makes GPS communication very susceptible to interference. Both unintentional RF interference (RFI) and purposeful hostile interference are detrimental to communications. Purposeful, hostile jamming is referred to as jamming (Rao (2012) Dovis (2015)).

1.3 The Application of Null-Forming Arrays

In signal compromised environments, the capability to combat RF interference (such as jamming) is necessary. A null in a radiation pattern is an area that has a low value of radiation pattern gain. The null represents the location in 3D space that an antenna would have very low gain in either transmit or receive modes. The objective of null-forming arrays is to create nulls at all locations of unwanted interference while still maximizing the gain at the directions of the desired signals. For the scenarios

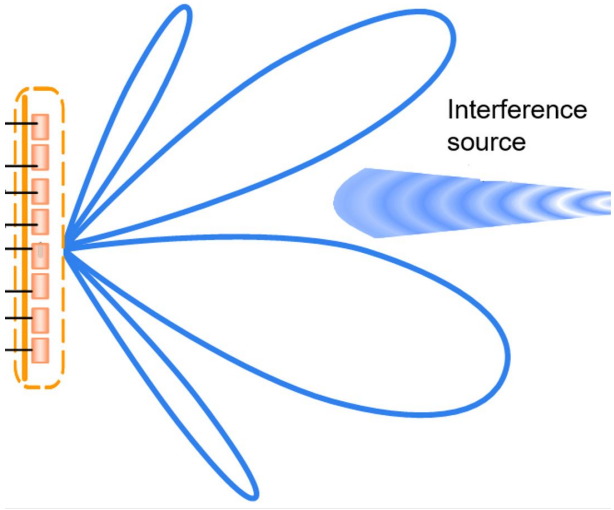

Figure 1.1: Null-forming array used to avoid interfering signals. (Wen et al. 2022)

discussed in this thesis it is assumed the locations of signals are known. Figure 1.1 shows a representation of a linear antenna array forming a null at a specific direction.

1.4 GNSS and FAA's Operational Missions

The FAA's flight inspection mission includes analysis of the navigation on the aircraft itself (Gondy 2002), testing of GPS-based approach procedure, as well as the inspection of GPS-based landing aide facilities. In a GPS-compromised environment (such as military tactical airport) however, anti-jamming capability would be needed. During an aircraft's take-off and especially the landing stage, there are multiple sources of interference affecting the navigation sensing systems, and they come from different azimuth and elevation directions as depicted in Figure 1.2 (Wolfley et al. 2022). The objective of this work is to aid flight inspection operations by visually examining the nulling patterns generated from anti-jamming arrays. It is significant that these visual formations are from the measured data and actual arrays made from GNSS antennas used in the field. The generated patterns are not simply simulated but are made from

practical data. The specific task herein is for both traditional flight inspection (FI) of civilian and military anti-interference operations.

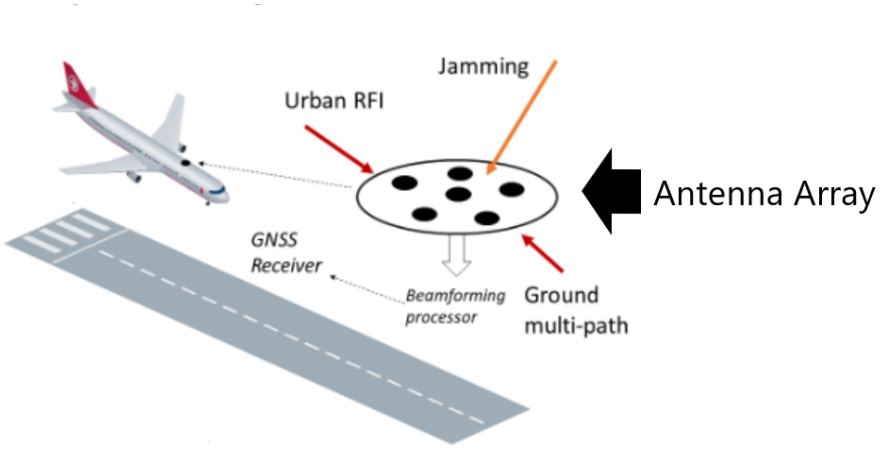

Figure 1.2: Scenario of anti-jamming GPS antenna operation. (Wolfley et al. 2022)

1.5 Thesis Outline

The characteristics of GNSS antennas will be discussed including analysis of circular polarization and transmission with both helical and linear transmit antennas. This document will evaluate the patch antennas made in-house and the commercial-off-the-shelf antennas. Also discussed will be the multiple array layouts used in this study.

An overview of analog beamforming methods will be given and the Butler matrix will be shown as an example. Digital beamforming will also be discussed for both 1D and 2D arrays. Also discussed will be weight calculations for adaptive null-forming techniques. The calculated weights will be applied to a simulated, synthesized and measured array.

The laboratory measurement setups will be discussed for the FF anechoic chamber and the NF anechoic chamber. Both NF, spherical, and X-Y planar modes will be

discussed. The set-up for both L1-band RHCP and S-band H-V-Pol arrays will be shared.

The results will then be reviewed and discussed. The measured radiation pattern of the analog null-forming is compared to the synthesized digital null-formations of the same array. Simulated, synthesized and measured null-formation are compared to evaluate how well the nulls were able to attenuate the unwanted signals while still having the main beam directed toward the desired signal.

Chapter 2

Background of GNSS

2.1 Global Navigational Satellite System (GNSS)

Included under the umbrella of GNSS is GPS which is the United State's global positioning system (Hofmann-Wellenhof et al. 2007), GLONASS which is Russia's system (Kumar et al. 2021), Galileo operated by the European Union (Benedicto et al. 2000), and COMPASS also known as Beidou which is operated by China (Montenbruck et al. 2013). The four global systems each have a different orbit radius and different inclinations. The inclination refers to the angle between the orbiting plane and the plane of the Earth's equator. For example, if a satellite had an orbit on the same plane of the equator, it would have an inclination of 0°. Similarly, if the orbiting plane was on the plane of the Earths axis, the inclination would be 90°. (FAA 2023, GPS.gov 2022 and Rao 2012)

Modern GPS has an orbit in-between GLONASS and Galileo with a radius of 26,560km (16,503.619 miles) and an inclination of 55°. A satellite in the GPS system has an orbit time of 11 hours and 57.96 minutes. The frequencies of GNSS span from 1.1GHz to 1.6GHz. This study focuses on the L1 and S bands which span from 1-2 GHz and 3-4GHz, respectfully, (Skolnik (2001)). The GNSS antennas used in this study have a center frequency of 1.57542 GHz and corresponding wavelength of 19.029cm. (FAA 2023, GPS.gov 2022 and Rao 2012)

Satellite navigation systems are divided into multiple broad categories. As the name of GNSS suggests it has global coverage whereas the category of RNSS (Regional Navigational Satellite System) only has regional coverage. RNSS provides coverage for general use purposes while SBAS (Satellite-Based Augmentation System) provides regional coverage for aviation-specific systems. GBAS which stands for Ground-Based Augmentation System is also aviation-specific and is a support system for SBAS. As the name suggests, GBAS is a system set up on the ground, local to the landing area of aircraft. (FAA 2023, GPS.gov 2022 and Rao 2012)

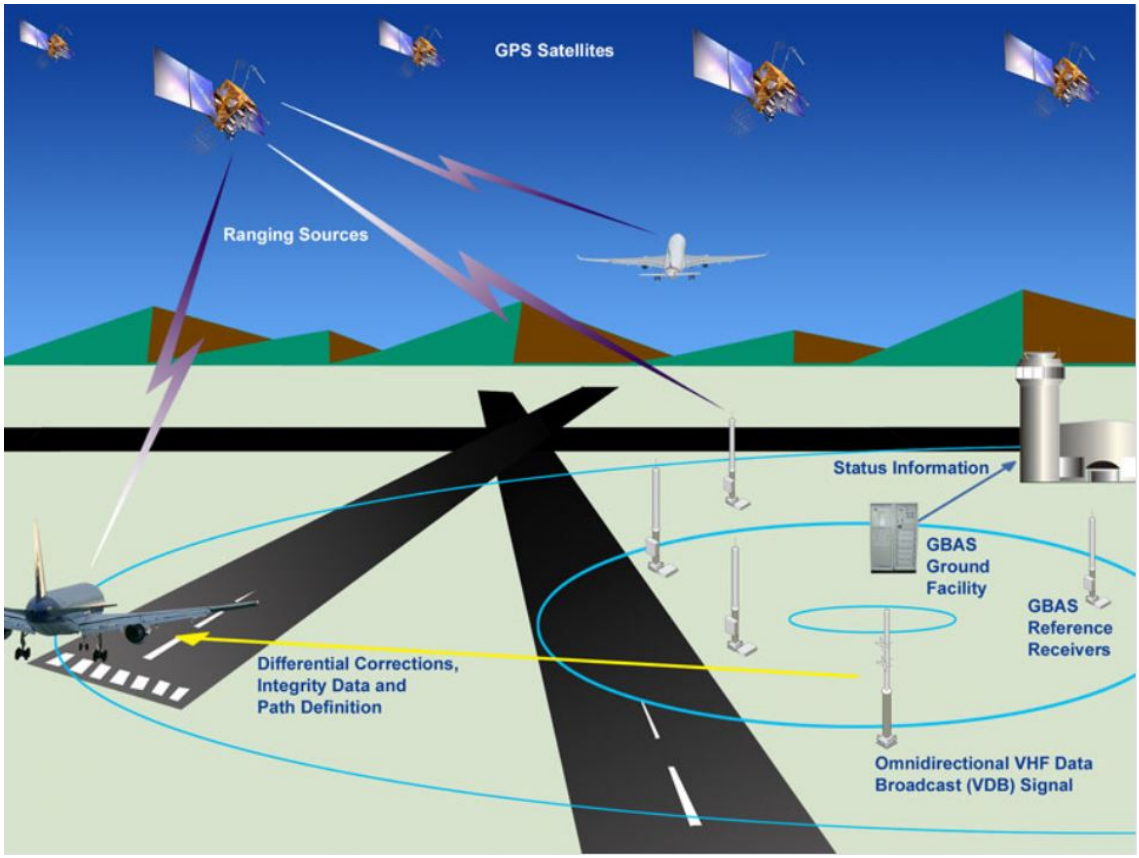

Figure 2.1: Architecture of a GBAS at an aircraft runway. (FAA 2023)

In the context of navigation systems, the word augmentation refers to an additional system that provides increased accuracy and other similar improvements to the navigation and timing of positioning systems. GBAS works in conjunction with GPS satellites to provide corrections to the landing approach of aircraft. A GBAS

facility uses the VHF radio link to communicate to GPS satellites. On the ground facility, there are reference antennas placed at known locations. A reference antenna is used to estimate the distance between itself and a GPS satellite from the measured transmission time of signals between the two. The estimated distances from each reference antenna and a GPS satellite are then compared with the known distances. After comparison, the error values can be determined. The average of the error values becomes the correction term that is applied to satellite ranges and used by GBAS avionics. The architecture of the GBAS facility is shown in Figure 2.1. (FAA 2023, GPS.gov 2022 and Rao 2012)

2.2 Polarization of GNSS Antennas

For GNSS antennas, circular polarization is preferred over linear polarization. For circular polarization, a receiving antenna is able to discriminate between direct signals and reflected signals from the multipath. This is because when a RHCP wave is reflected off an interface, its polarization changes to LHCP. This difference allows the receiving antenna to distinguish between direct signals and unwanted multipath signals. LHCP is the cross-polarization of the GNSS antenna and RHCP is the dominant polarization referred to as c-polarization. Cross-polarization is unwanted and the measured values should be much less than the Co-polarization. (Rao 2012 and Langley 1998)

The radiation pattern of circular polarization can be expressed by these two orthogonally polarized vector components along the unit vector directions $\hat{\boldsymbol{\theta}}$ and $\hat{\boldsymbol{\phi}}$ in spherical coordinates. These two components for the electric field are $\vec{E}_{\hat{\boldsymbol{\theta}}}$ and $\vec{E}_{\hat{\boldsymbol{\phi}}}$. Both RHCP and LHCP in linear magnitude can be written in terms of these components for the far-field radiated electric field. (Rao 2012)

$$RHCP = \vec{E}_{\hat{\boldsymbol{\theta}}} - j\vec{E}_{\hat{\boldsymbol{\phi}}} \tag{2.1}$$

$$LHCP = \vec{E}_{\hat{\boldsymbol{\theta}}} + j\vec{E}_{\hat{\boldsymbol{\phi}}} \tag{2.2}$$

$$\vec{E}_{\boldsymbol{\phi}} = E_{\boldsymbol{\phi}}(\frac{1}{\sqrt{2}})e^{-j\boldsymbol{\phi}} \tag{2.3}$$

$$\vec{E}_{\boldsymbol{\theta}} = E_{\boldsymbol{\theta}}(\frac{1}{\sqrt{2}})e^{-j\boldsymbol{\theta}} \tag{2.4}$$

Where $\boldsymbol{\theta}$ and $\boldsymbol{\phi}$ are phase shifts in radians and then $E_{\boldsymbol{\theta}}$ and $E_{\boldsymbol{\phi}}$ are both magnitudes of the electric field in units of (V/m).

2.3 Passive Patch Antenna

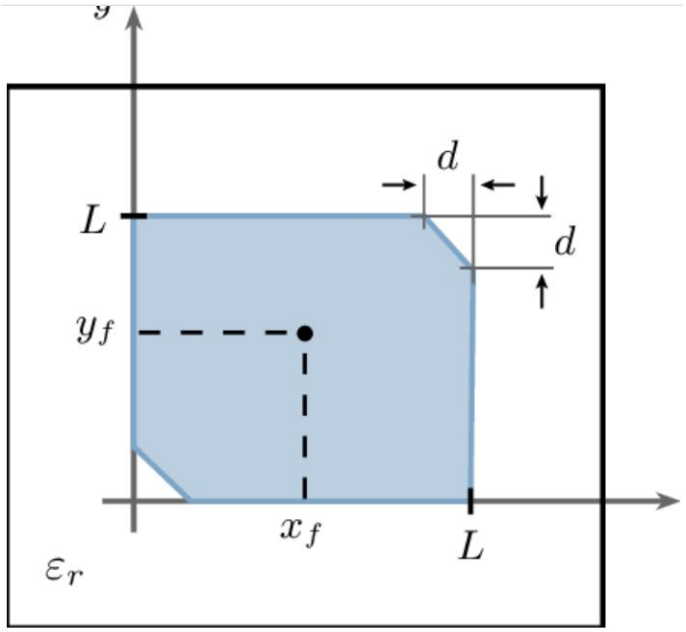

Figure 2.2: Circularly Polarized Patch Antenna with Cornered Edges. (La Valle et al. 2019)

GPS antennas are often made by patch antennas since they have a broad beamwidth. A broad beamwidth is necessary for an receiver to acquire at least four satellites at a time, which is a performance requirement for GNSS antennas. The microstrip (MS)

patch antenna is suitable for aircraft and satellite applications for many physical reasons including its conformability to planar and non-planar surfaces, and low-cost fabrication procedure. The construction consists of a metallic patch laying on a dielectric substrate which is grounded by a ground-plane. The metallic patch can be fed with many different orientations including edge fed, series fed, or corporate fed. The patch antennas in this study have a center probe feed. The location of the center feed can determine the polarization of the antenna. The shape of the patch can be square, square with trimmed edges, circular or elliptical. The desirable EM characteristics of a MS patch include low cross-polarization and its radiation pattern which has a large beamwidth. MS patch antennas are very versatile in design and can be made for linear and circular polarizations, various radiation patterns, and a large range of resonant frequencies. (Balanis 2005 and Rao 2012)

All GNSS antennas shown in this thesis are RHCP passive L-1 GPS antennas designed for a center frequency of 1.575 GHz and a corresponding wavelength of 19 cm. The microstrip RHCP antennas in this study are of the cornered edge design where two opposite corners are trimmed as shown in Figure 2.2. (Balanis 2005)

This study generates simple example array designs mainly for learning and demonstration, which are further described in Chapter 3.

Chapter 3

Antennas Used in This Study

3.1 Helical Antenna

A helical antenna is a type of directional antenna with narrow beamwidth, and it is used for the transmitting test antenna for both near and far-field ranges. A typical helical antenna generates RHCP or LHCP waves using the structure as described in the book GPS/GNSS Antennas by Rao (2012). A cylindrical axial mode helix antenna is used in our studies. Because of the large size of these types of antennas, they are not usually used as receivers but are sometimes used as stationary transmit GPS antennas. Figure 3.1 shows a helical antenna set up for transmit mode in the near-field chamber.

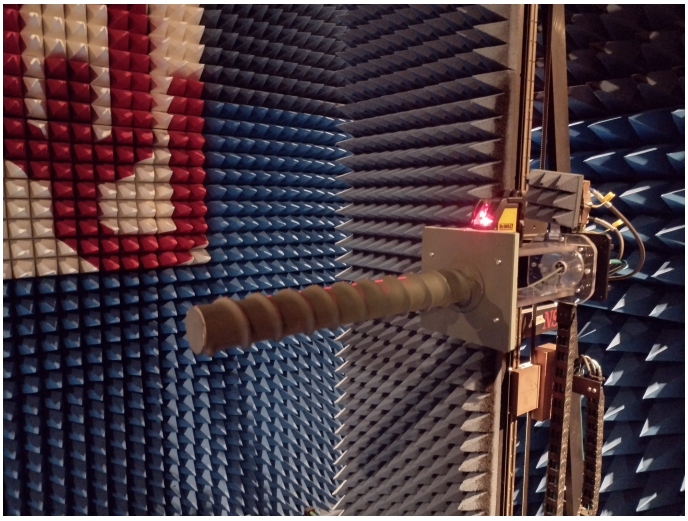

Figure 3.1: Cylindrical axial mode helix antenna.

3.2 Rectangular Waveguide

A rectangular waveguide was used as the transmitter for the S-Band antenna measurements. Characteristics of waveguide antennas can be found here Cheng (1989). Figure 3.2 shows the antenna in the near-field chamber set up for X-Y planar mode. Figure 3.2 (a) shows the antenna in position to transmit vertical polarization (V-Pol). Figure 3.2 (b) shows the antenna in position to transmit horizontal polarization (H-Pol).

(a) 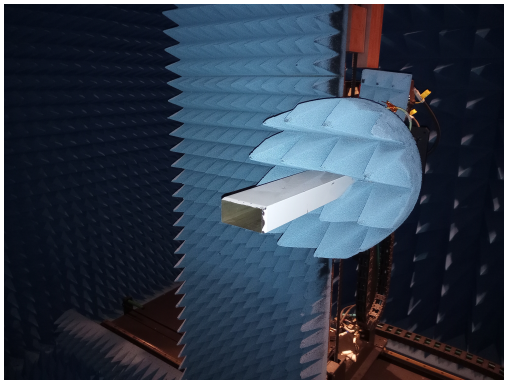 (b) 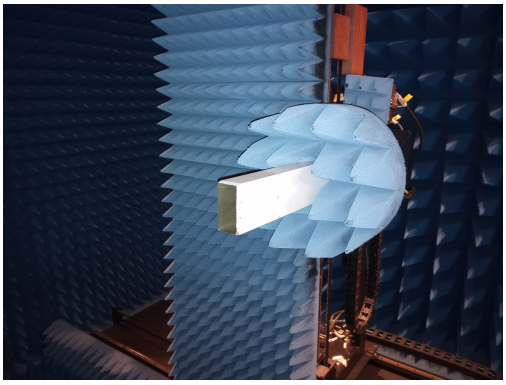

Figure 3.2: Rectangular waveguide TX antenna (a) V-Pol transmit, (b) H-Pol transmit.

3.3 In-House GNSS Antenna

Figure 3.4 shows fabrication of an in-house design of a microstrip patch antenna. The design is a square micro-strip patch antenna that has cornered edges for RHCP. The antenna is center-fed. The design was fabricated on single-layer Rogers RO4350B substrate. The dimensions are designed for center frequency of 1.575 GHz.

3.4 Commercial-off-the-shelf GNSS Antennas

L1 band RHCP patch antennas were sourced from a company named GPS Source. The model name of the antennas is L1P. The pass band was 1.56 GHz to 1.59 GHz and a nominal gain of 3 dBi. The antennas were encased in a plastic housing with a bottom mount with a center fed SMA connector. Figure 3.3 shows a commercial off-the-shelf patch antenna that was removed from a black casing that it came in.

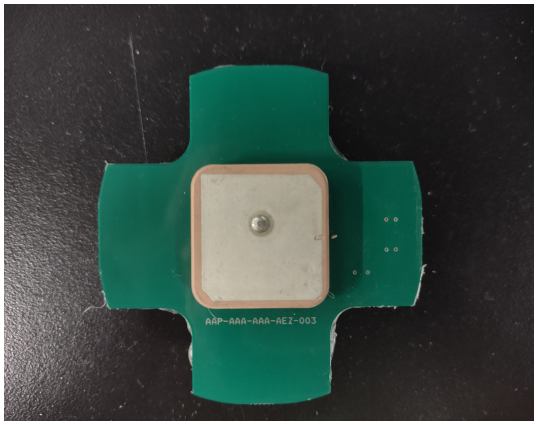

Figure 3.3: Single element patch antenna - vendor provided.

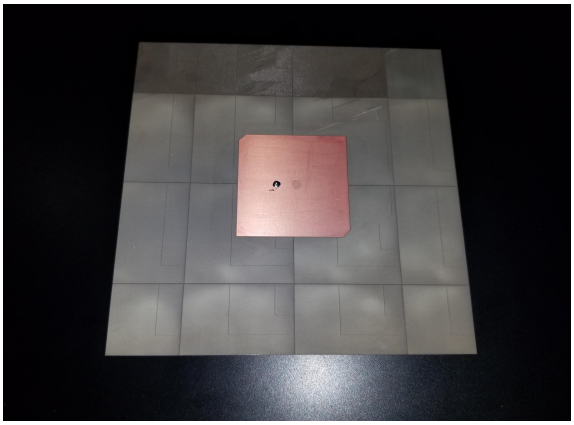

Figure 3.4: Single element patch antenna - in-house design and fabrication.

3.5 Linear Array with GNSS Antenna Elements

A 6-element uniform linear array (ULA) was constructed with commercially bought RHCP patch antennas. All elements share a ground plane. The distance from the edge of all elements to the edge of the ground-plane is at least half a wavelength. The spacing between the elements from center to center is half a wavelength. Resonant frequency is 1.575 GHz. The array is shown in Figure 3.5.

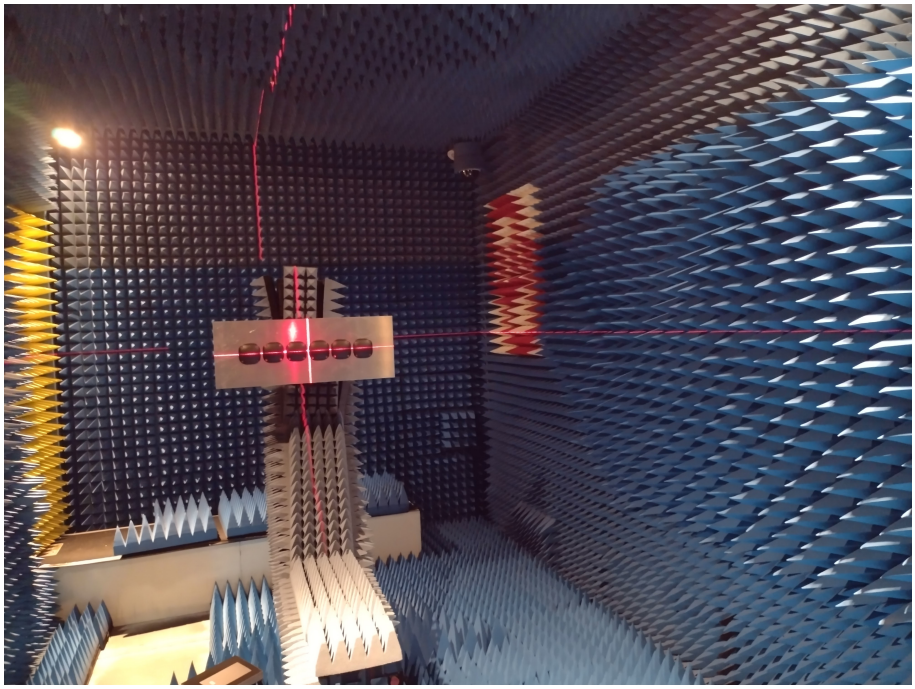

Figure 3.5: 6 Element ULA in near-field chamber setup for spherical mode.

3.6 Planar Arrays

3.6.1 2 By 3 Planar Array

A 2 by 3 planar array was constructed with commercially bought RHCP patch antennas. All elements share a ground plane. The distance from the edge of all elements to the edge of the ground-plane is at least half a wavelength. The spacing between

the elements from center to center is half a wavelength. Resonant frequency is 1.575 GHz. The array is shown in Figure 3.6.

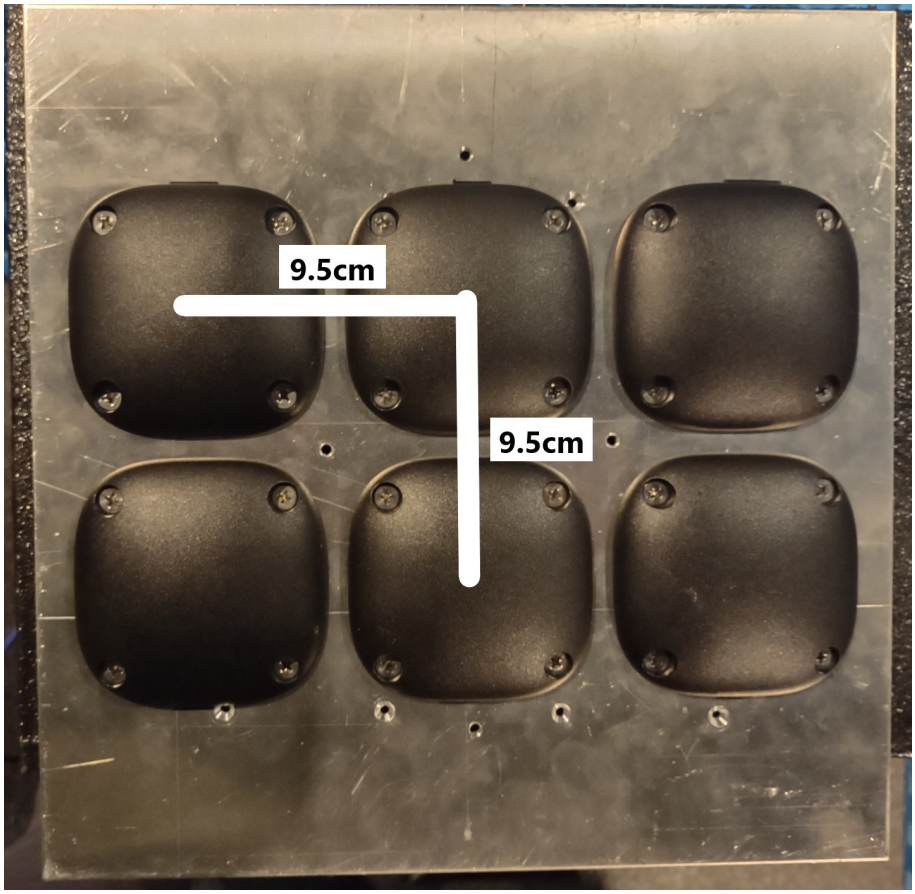

Figure 3.6: 2 by 3 GNSS array with 0.5λ spacing between elements.

3.6.2 Circular Planar Lattice

The circular planar lattice is composed of seven identical elements, each element has half-wavelength spacing from surrounding elements. There is a shared ground-plane for all antennas. The distance from the edge of all elements to the edge of the ground-plane is at least half a wavelength. The elements are the commercially off the shelf RHCP patch antennas. Resonant frequency is 1.575 GHz. The array is shown in Figure 3.7.

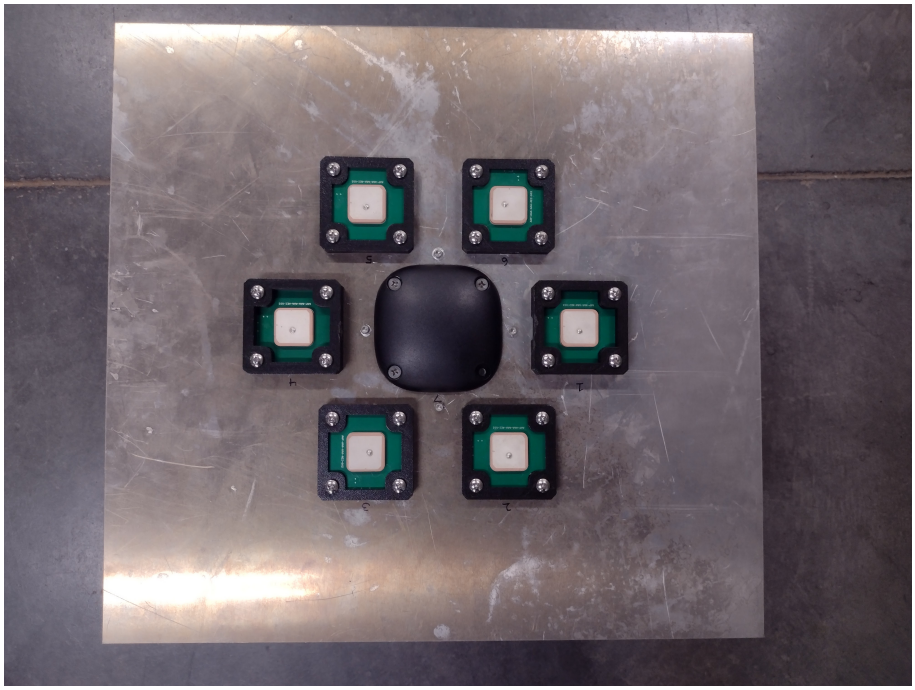

Figure 3.7: 7-Element GNSS circular array with 0.5λ spacing between elements.

3.6.3 S-Band Rectangular Array

An S-band (operating at 3 GHz) rectangular array antenna was also used with only the top row enabled, thus functioned as an 8-element, vertical polarized ULA with a half-wavelength lattice (Figure 3.8). Each element is controlled by a MATLAB GUI through a phase and amplitude control (PAC) board so different beamforming/null-forming solution can be tested. This array is only for reference studies in this thesis and for verification of beamforming methods.

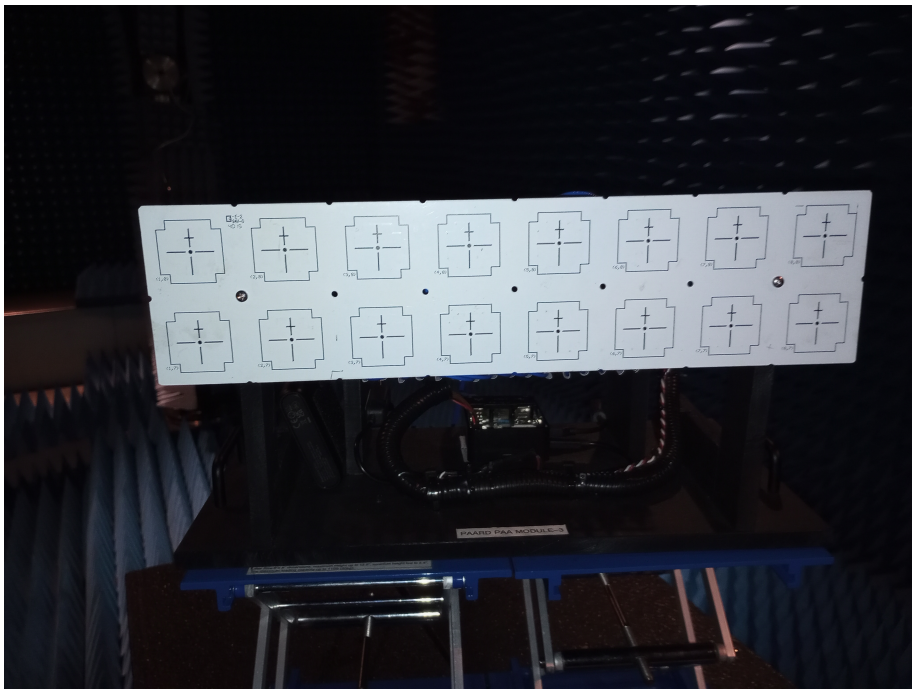

Figure 3.8: A 2 by 8 S-Band array with 0.5λ spacing between elements.

Chapter 4

Phased Array Characteristics and Beamforming Algorithm

Phased array radars are utilized for their beamforming abilities. Beamforming is the ability to electronically modify the direction of an antenna's boresight. The pattern of an antenna can be customized in such a way to maximize the reception of the signals of interest (SOI) and decrease the reception of the signals not of interest (SNOI). The main beam of an antenna array is directed toward the SOI while attenuating the signals coming from other directions. The term "beamforming" includes both null forming and beam-steering techniques. Beam-steering is the steering of the main lobe of the antenna pattern. A null is an area in the antenna pattern with a minimized gain. There are many different variations of phased array antennas including linear, rectangular, and circular lattice arrays.

4.1 Linear Array

This section discusses the characteristics of linear arrays. The equations for electric field and gain are shown with ideal conditions. Excitation errors are not considered. Equation 4.1 gives the electric field for both a linear and planar array as described in Salazar (2022).

$$\overline{E}(\theta) = \overline{E}_O(\theta) \cdot AF(\theta), \tag{4.1}$$

where $\overline{E}_O$ is the pattern of a single element also known as the embedded element pattern and AF is the array factor. The AF is a scaling factor for the embedded element pattern as shown in figure 4.1. The AF is only dependant on the number of elements and the spacing between them. It is not dependent on the type of element or its pattern. Equation 4.2 defines the AF for a linear array. The AF is further described here EMViso (2021a) and here Salazar (2022).

$$\mathrm{AF}(\theta) = \sum_{n=1}^{\mathrm{N}} e^{j(n-1)(kdcos\theta+\beta_x)} \tag{4.2}$$

In equation 4.2, $k = \frac{2\pi}{\lambda}$ is the wave number and λ is the wavelength of the propagating signal. It is important to note that θ is not the steering angle but it is the observation angle in the elevation plane. Also, n is the number of elements in the array. The variable d is the distance between the individual elements on the x axis. For 0.5λ distancing, $kd = \pi$ and if the phase component, β_x, is set to zero, then the embedded element pattern multiplied by the array factor simplifies to the form below.

$$\overline{E} = \overline{E}_O \sum_{n=1}^{\mathrm{N}} e^{j(n-1)(\pi cos\theta)} \tag{4.3}$$

$$\overline{E} = \overline{E}_O \sum_{n=1}^{\mathrm{N}} e^{j(n-1)\psi} \tag{4.4}$$

To find the maximum electric field of a uniform linear array, $\overline{E}_{max}$, the phase component of equation 4.4 is set to zero. This is because the beam is maximum when phase is zero $\psi = 0$. Therefore, $e^{j(n-1)\psi} = 1$ and $\overline{E}_{max}$ is simplified to equation 4.5 as described here Salazar (2022)

$$\overline{E}_{max} = \overline{E}_o \sum_{n=1}^{\mathrm{N}} 1 = \overline{E}_o N \tag{4.5}$$

The equation for the gain of an N element linear array is shown below. All N elements are along the x-axis.

$$G = \frac{4\pi(N_x d_x) cos\theta_o (1 - |\mathbf{\Gamma}|^2)\epsilon_t}{\lambda^2}, \tag{4.6}$$

where $\mathbf{\Gamma}$ is the active reflection coefficient, θ_o is the scanning angle, d_x is the distance between elements, λ is the wavelength of the propagating signal and ϵ_t is the total efficiency of the array. For a uniform array, ϵ_t is 1. (Salazar 2022)

The gain loss can be reduced if the reflection coefficient decreases. As shown in equation 4.6, as the reflection coefficient gets larger, the gain loss gets larger as well. The reflection coefficient is a value of how much power goes from the source and is returned back to the source. The difference between an active reflection coefficient and a passive reflection co-efficient is that the active reflection coefficient is angle dependent and considers frequency and the passive does not. For a uniform linear array, equation 4.5 can be used for a simplified form for gain estimation as shown in 4.7. (Salazar 2022)

$$G \approx |\overline{E}_{max}|^{2.} \tag{4.7}$$

4.2 Planar Array

This section discusses the figures of merit for planar arrays. Equation 4.8 shows the beam-forming algorithm that uses a conventional radiating element weighting to steer the main beam. The antenna pattern is function of both θ and ϕ which are the observation angles for the elevation and azimuth planes respectively. Shown in equation 4.9, the variables β_x and β_y are the phase components which enable steering

of the beam. In equations 4.10 and 4.11, θ_O is the steering angle in the elevation angle, ϕ_O is the steering angle in the azimuth plane. The typical intention of steering is to maximize gain towards signals of interest (SOIs) and to create nulls in the direction of signals not of interest (SNOIs). The total output pattern of the array will be denoted as $\overline{E}$ and the radiation pattern of an individual element will be denoted as $\overline{E}_O$ also known as the embedded element pattern. For an array with M columns and N rows, the 3D beamforming equation for the planar array is given in equation 4.8. (Balanis 2005 and Salazar 2022)

$$\overline{E}\left(\theta,\phi\right) = \overline{E}_O\left(\theta,\phi\right) \cdot AF\left(\theta,\phi\right) \tag{4.8}$$

The variable AF in equation 2.1 represents the array factor (Balanis 2005) for a uniform planar array, which is given by the equation 4.9. Uniform in this context means the elements of the array are the same and they have uniform amplitude and phase excitation. The AF is a scaling factor as shown in figure 4.1. The AF is dependent on the number of elements and the spacing between them. It is not dependent on the type of element. (EMViso 2021a, EMViso 2021b and Balanis 2005)

$$\mathrm{AF}(\theta,\phi) = \sum_{n=1}^{\mathrm{N}} e^{j(n-1)(kd_x sin\theta cos\phi+\beta_x)} \sum_{m=1}^{\mathrm{M}} e^{j(m-1)(kd_y sin\theta sin\phi+\beta_y)} \tag{4.9}$$

$$\beta_x = -kd_x sin\theta_O cos\phi_O \tag{4.10}$$

$$\beta_y = -kd_y sin\theta_O sin\phi_O \tag{4.11}$$

In equations 4.9 - 4.11, the variables d_x and d_y are the relative positions of the individual elements in x and y coordinates, respectively. The variables β_x and β_y are the phase components which enable steering of the beam. In equations 4.10 and 4.11, θ_O is the steering angle in the elevation angle, ϕ_O is the steering angle in the azimuth

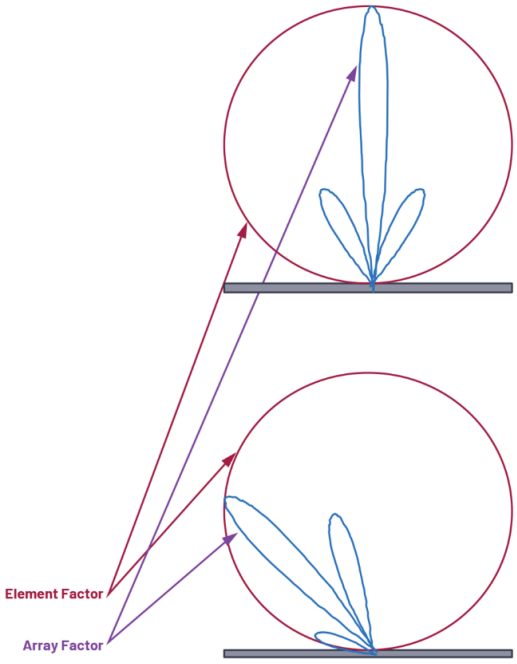

Figure 4.1: The Array Factor in equation 4.8 shown as a scaling factor of the elements radiation pattern. (Delos et al. 2020)

plane. Equation 4.9 can be applied to linear, rectangular, and circular lattice arrays. (Balanis 2005)

The gain for a rectangular planar array is given in equation 4.12 and the directivity is given by 4.13. Gain and directivity are related by the value of ϵ_t which is the total efficiency of the array. For a uniform array ϵ_t is zero which means the directivity is equal to the gain for an ideal uniform array. (Salazar 2022)

$$G = \frac{4\pi(N_x d_x M_y d_y) cos\theta_o (1 - |\mathbf{\Gamma}|^2)\epsilon_t}{\lambda^2} \tag{4.12}$$

$$D = \frac{G}{\epsilon_t} = \frac{4\pi(N_x d_x M_y d_y) cos\theta_o (1 - |\mathbf{\Gamma}|^2)}{\lambda^2}, \tag{4.13}$$

where $\mathbf{\Gamma}$ is the active reflection co-efficient, θ_o is the scanning angle and d_x is the distance between elements.

Using equation 4.9, the radiation pattern was simulated for an 8 by 8 planar array as shown in figure 4.2. This is with uniform distribution. The peak side-lobe level is -13 dB. Gain and directivity were calculated and shown on the figure. For an array with uniform distribution, the total efficiency is 1 which causes the gain and directivity to be equal. (Salazar 2022)

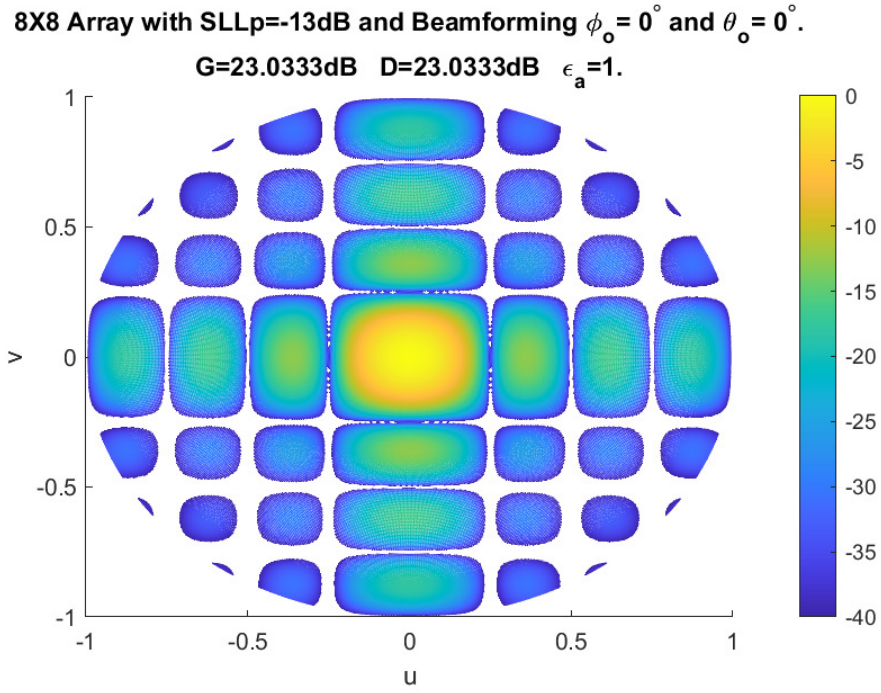

Figure 4.2: Beam pattern of an 8 by 8 planar array with uniform weighting.

Results of 2D beamsteering using the rectangular array lattice is shown in Figure 4.4. The beam was shifted 20° in ϕ and 10° in θ. The main lobe shifts from boresight (ϕ_O= 0° and θ_O= 0°) to the scanning location (ϕ_O= 20° and θ_O= 10°). Figure 4.3 compares two theta cuts observed at $\phi = 90°$ and $\phi = 0°$ for uniform weighting. Figure 4.5 compares the same theta cuts after beamforming weights are applied for $\phi_O = 20°$ and $\theta_O = 10°$.

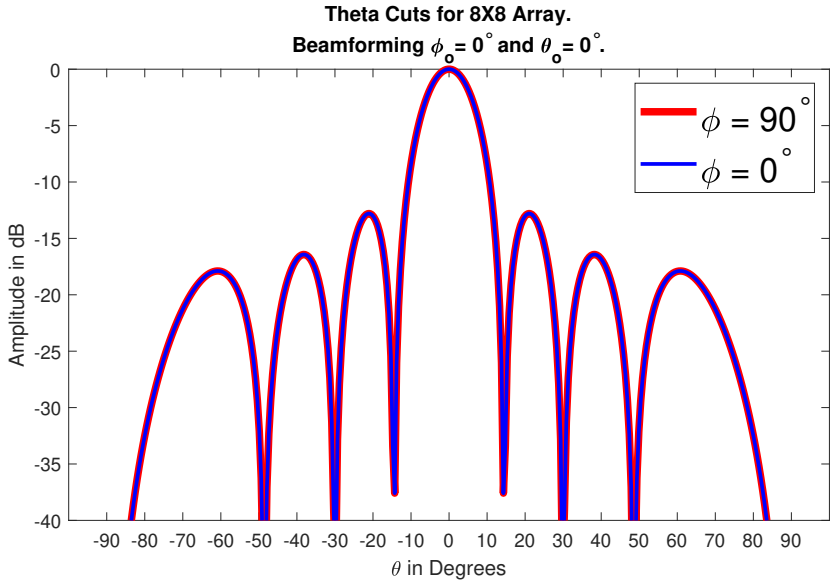

Figure 4.3: Comparison of theta cuts observed at $\phi = 90°$ and $\phi = 0°$. Uniform beamforming of 8 by 8 planar array $\phi_O = 0°$ and $\theta_O = 0°$.

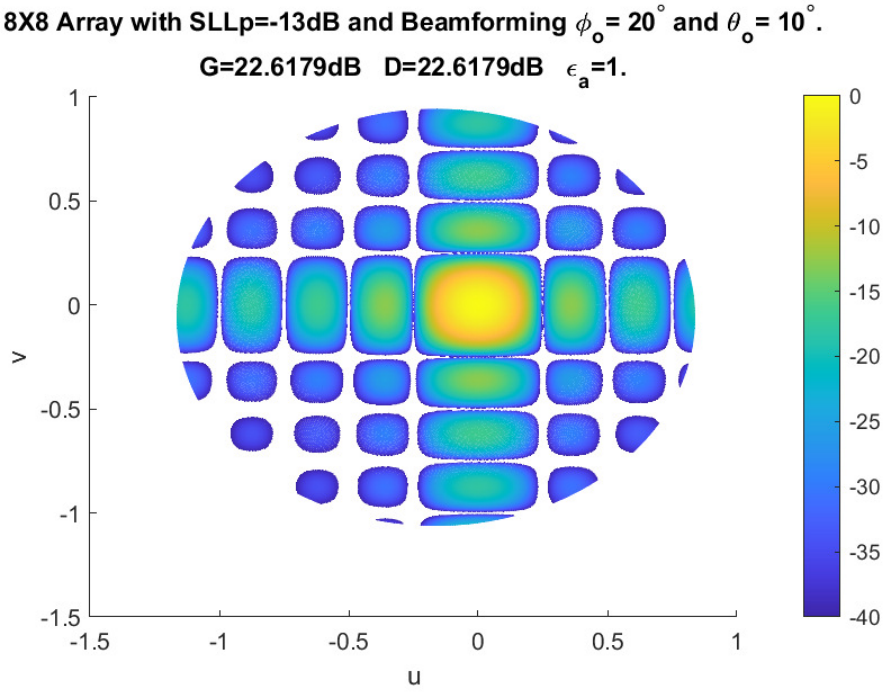

Figure 4.4: Beam steering of 8 by 8 planar array for $\phi_O = 20°$ and $\theta_O = 10°$.

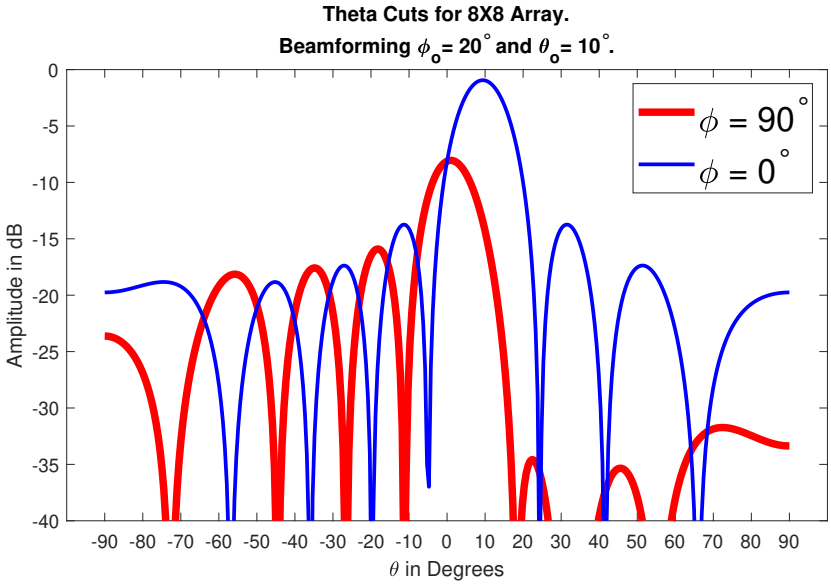

Figure 4.5: Comparison of theta cuts observed at $\phi = 90°$ and $\phi = 0°$. Beamforming of 8 by 8 planar array $\phi_O = 20°$ and $\theta_O = 10°$.

Chapter 5

Analog and Digital Beamformers

5.1 Beamforming Methods

There are analog and digital methods for beamforming which have unique characteristics but produce similar array radiation patterns. Both methods effectively apply a complex weight to each of the array elements and then sum them together. With analog beamforming, the amplitude and phase weights are applied before analog to digital conversion (ADC) of the received power. With digital beamforming, the received power is digitized before amplitude and phase weights are applied. The difference in the ADC timing is evident when comparing the processes in Figure 5.1 and Figure 5.3. The beamforming algorithm shown in equation 4.8 applies to both analog and digital BF methods. (Balanis, 2005 and WirelessWorld, 2012 and Skolnik, 2001)

5.2 Analog Beamforming

A beam-former applies a complex weight to each of the array elements and then sums them together. Figure 5.1 shows the individual weights applied before the power combiner and before any digitizing happens. The complex weights are denoted as $\mathbf{w}$ and θ and $\mathbf{a}$ are the phase and amplitude components of the complex weights. With analog beam-forming, the manipulation of the phase and amplitude of each element is

applied with analog hardware that feeds the array. The hardware could include field programmable gate arrays (FPGAs) (Shelley et al., 2010), PAC boards, or switching networks. (WirelessWorld, 2012 and Skolnik, 2001)

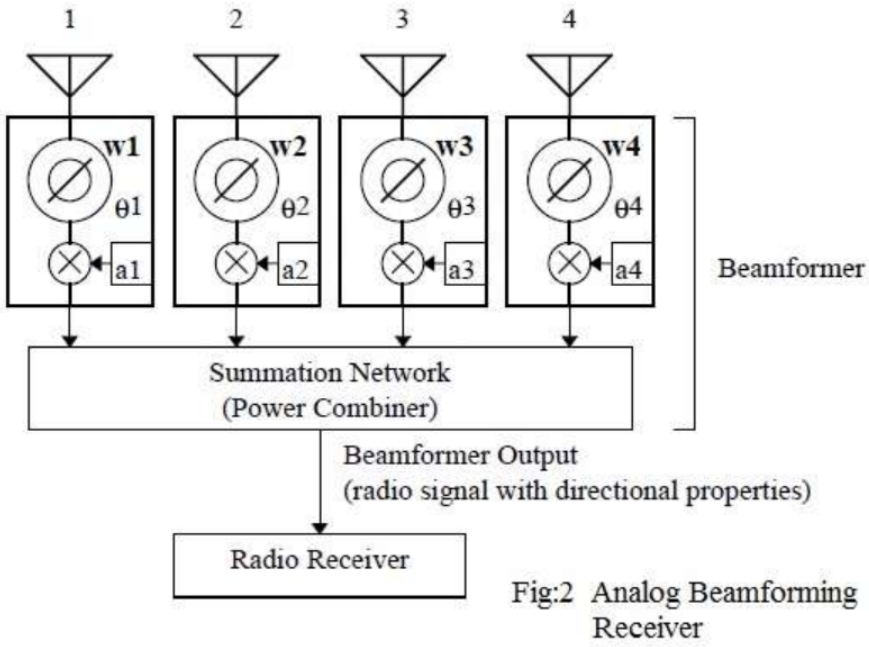

Figure 5.1: Analog beamforming receiver. (WirelessWorld, 2012)

5.2.1 Discussion of Butler Matrix

As one example of analog beamforming, a specific switching network will be discussed in this section. The Butler Matrix switching network is comprised of micro-strip quadrature couplers and fixed phase shifters. There are four input ports and four output ports connected to the array antennas. The switches in the Butler Matrix determine which input port is excited. Only one port is excited at a time. The excited port determines the direction of the beam that is formed from the array. Since there are four ports that can be excited, there are four different directions for the beam to be steered. The position of the individual beams is determined by the fixed phase shifters. The number of different beam directions is equal to the number

of input ports which is also equal to the number of output ports. A schematic of a 4-element Butler Matrix is shown in a blog published by COSMOL in 2017 (Fairclough, 2017). Skolnik's work on radar systems provides an explanation of an eight-element Butler beamforming matrix. (Skolnik, 2001, Fairclough, 2017, Lopez La Valle, 2019, and S. Kim and Shin, 2019)

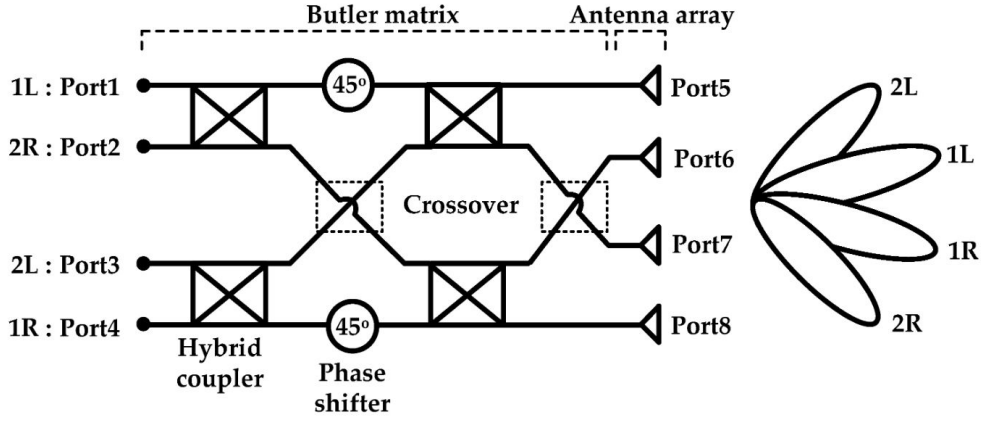

Figure 5.2: Eight-port Butler Matrix layout. (S. Kim and Shin, 2019)

5.3 Digital Beamforming

A digital beamformer converts the received power of each receiving element from an analog signal to a digital signal before applying the complex weights and summing them together for synthesis. Figure 5.3 shows the individual weights applied after conversion to digital happens. The complex weights are denoted as $\mathbf{w}$ and θ and a are the phase and amplitude components, respectively, of the complex weights. (Skolnik, 2001 and WirelessWorld, 2012)

It is very common for phased array radars (PARs) to utilize digital beamforming. The digital processors that apply the weights to the RX/TX elements can be re-programmed and updated for sustainability. Digital beamformers are expected to have better versatility than analog beamformers are not. (Skolnik, 2001)

$$\mathbf{w}_{nm} = a_{nm}e^{j\beta} \tag{5.1}$$

$$\beta = \beta_x + \beta_y = -(kd_x sin\theta_o cos\phi_o + kd_y sin\theta_o sin\phi_o) \tag{5.2}$$

$$\mathbf{w}_{mn} = a_{nm}e^{-j(kd_x sin\theta_o cos\phi_o + kd_y sin\theta_o sin\phi_o)} \tag{5.3}$$

$$\mathbf{w}_{mn} = a_{nm}e^{-j\pi(nsin\theta_o cos\phi_o + msin\theta_o sin\phi_o)} \tag{5.4}$$

The variable β is the phase component of the complex weight which controls the steering direction of the beam. In equation 5.2, θ_o is the steering angle in the elevation angle, ϕ_o is the steering angle in the azimuth plane. The variable a is the amplitude excitation for each element. Equation 5.4 shows the complex weight for a planar array that has elements that are all 0.5λ apart from each other. This causes the following simplifications: $kd_x = n\pi$ and $kd_y = m\pi$. (Balanis, 2005)

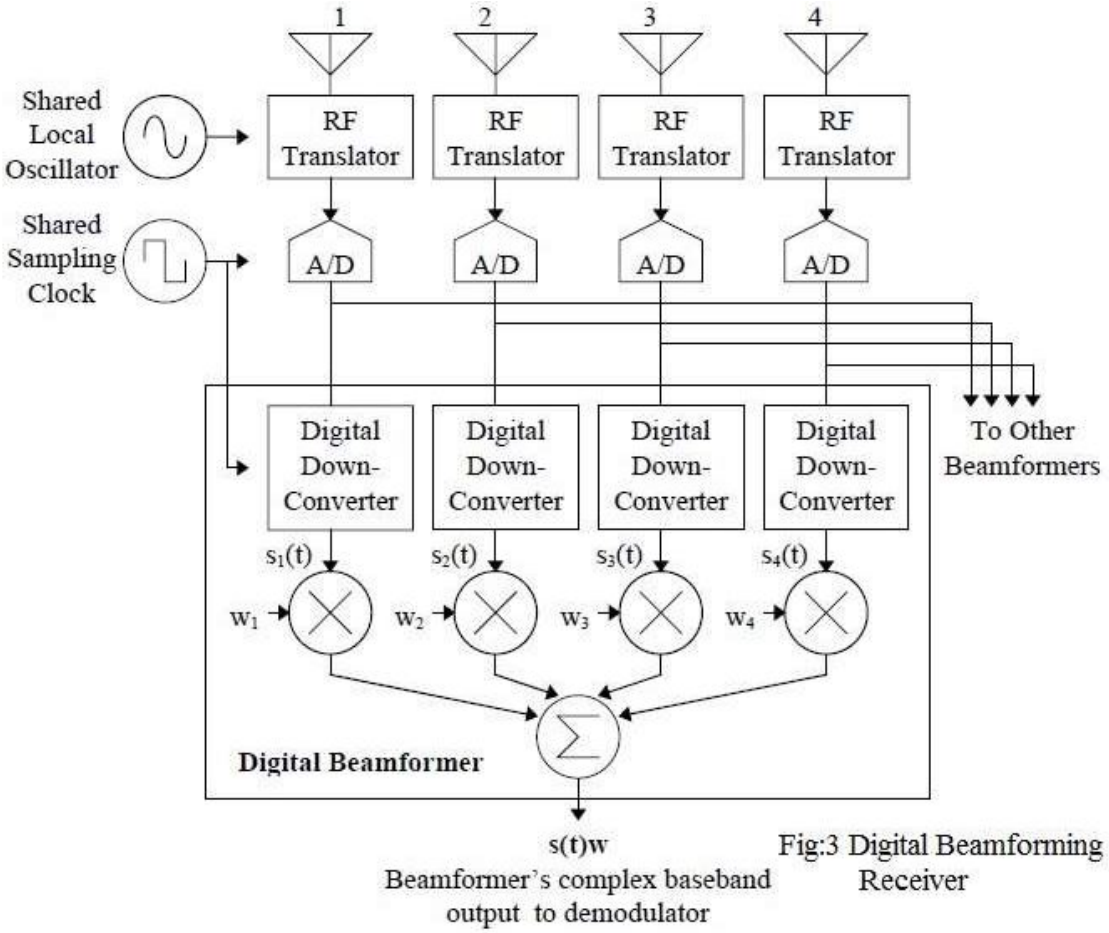

Figure 5.3: Digital beamforming receiver. (WirelessWorld, 2012)

Chapter 6

Adaptive Null-Forming Techniques

6.1 Null-Forming

Null-forming is minimizing the gain in the directions of interference while maximizing the gain in the direction of the desired signal. After each element of the array is measured in the anechoic chamber, in post-processing, nulling techniques generate weighted vectors based on locations of interference and the direction of the SOI. The weighted vectors are applied digitally to the synthesized array and then were applied to the analog or digital phase and amplitude controller. The measured radiation pattern of the analog null-forming was compared to the synthesized digital null-formations of the same array. The goal is to observe how well the nulls are able to attenuate the unwanted signals while still having the main beam directed toward the desired signal. There are many adaptive beamforming methods many of which are discussed in a book by Henry Van Tress named Optimum Array Processing (Van Trees, 2002). Methods of adaptive null-forming are discussed below including side-lobe canceler method and the covariance matrix method.

6.2 Sidelobe Canceller Method

One of the simplest algorithms to form nulling weights is the side-lobe canceller method. This method assumes that the locations of the desired and unwanted signal are known. First, the steering vector of the unwanted signal is calculated and then scaled. The scaling factor is computed from the response of the SOI at the null location as shown in Equation 6.1. The scaled steering vector is then subtracted from the steering vector of the desired signal (or SOI) as shown in Equation 6.2. The symbol $\odot$ denotes element-wise multiplication. (Monteiro 2015, Mathworks 2023a and Priyanka and Vishnu 2011)

$$w_o = \text{steering vector for signal of interest (SOI)}$$
$$w_x = \text{steering vector for signal not of interest (SNOI)}$$
$$w_x' = \text{complex conjugate transpose of } w_x$$
$$w_o' = \text{complex conjugate transpose of } w_o$$
$$r = \text{response of the SOI at the SNOI location}$$
$$\mathbf{W} = \text{null-forming weight}$$

$$\mathbf{r} = [w_x' \odot w_o]^{-1}[w_x' \odot w_x] \tag{6.1}$$

$$\mathbf{W} = w_o - (w_x \odot r) \tag{6.2}$$

Figures 6.1 and 6.2 show the results when this method is applied to the 1 by 3 array with the GNSS elements, as shown in Figure 3.3. The array was measured in the NF chamber using spherical mode scanning. The radiation patterns of the elements were measured individually and then synthesized in post-processing. The weights for each element were calculated using the sidelobe canceller method and then applied to the synthesized patterns. A gain of -20 dB is desirable at the location of a signal not of interest (SNOI). A gain of 0dB is desirable at the location of the SOI.

The nulls produced in scenarios of figures 6.1 and 6.2 range from -12 dB to -35 dB. The depths of the nulls are reasonable, however, the deepest part of the null is not always at the exact location of the SNOI, as shown in Figures 6.1 (b) and 6.2 (b). The nulls could possibly be shifted toward the more accurate SNOI direction with further optimizations.

(a) 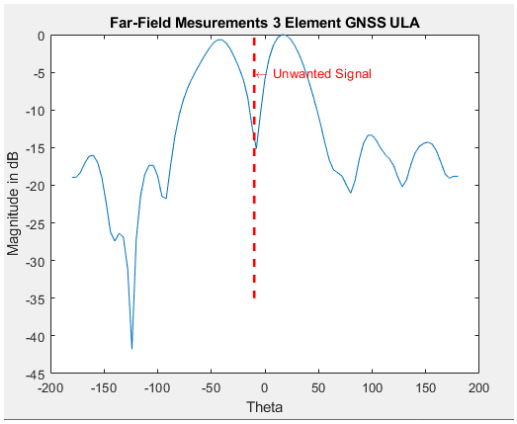

(b) 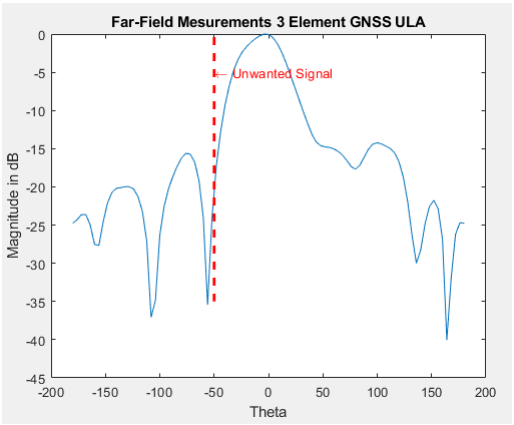

Figure 6.1: Preliminary results of Sidelobe canceler method applied to a synthesized 3-element linear array (a) SNOI at $\theta = -10^{\circ}$ (b) SNOI at $\theta = -50^{\circ}$

(a) 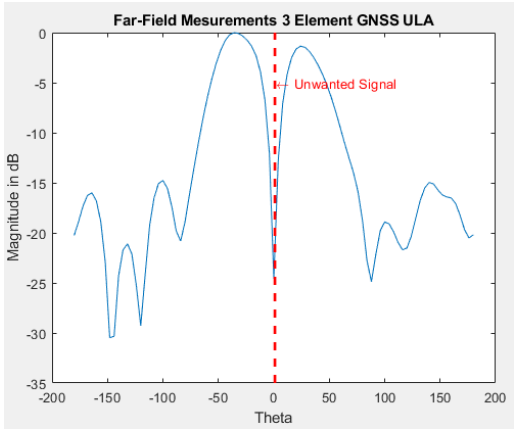

(b) 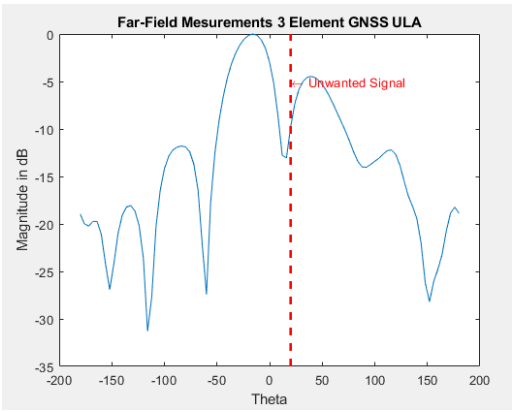

Figure 6.2: Preliminary results of Sidelobe canceler method applied to a synthesized 3-element linear array (a) SNOI at $\theta = 0^{\circ}$ (b) SNOI at $\theta = 20^{\circ}$.

6.3 Covariance Matrix Method

Equation 6.3 defines a covariance matrix (Cuesll 2023, Kolman 2008). A covariance matrix is square and symmetric which means the transpose is equal to the original matrix, as shown in equation 6.4. The main diagonal of the matrix contains the sample variance values. Equation 6.5 shows the equation for variance between the data and equation 6.6 defines the covariance of a data set. Examples of the covariance matrix being applied to antenna array design/analysis are provided in Gregory et al. (2011) and Bose et al. (2021). (Cuesll 2023 and Kolman 2008)

$$\mathbf{R} = \begin{bmatrix} Var(x_1) & ... & Cov(x_1, x_n) \\ : & ... & : \\ Cov(x_n, x_1) & ... & Var(x_n) \end{bmatrix} \tag{6.3}$$

$$\mathbf{R^T} = \mathbf{R} \tag{6.4}$$

$$Var(x) = \frac{\sum_1^n (x_i - \overline{x})^2}{n-1} \tag{6.5}$$

$$Cov(x, y) = \frac{\sum_1^n (x_i - \overline{x})(y_i - \overline{y})}{n-1} \tag{6.6}$$

$\overline{x}$ = mean in dataset x

x_i = observation in dataset x

$\overline{y}$ = mean in dataset y

y_i = observation in dataset y

n = number of values in datasets (both datasets should have the same number)

Covariance of interference can be found using equation 6.3. Its inverse is taken and multiplied by the steering vector of the SOI (equation 6.7). The algorithm for finding the total weighted sum of all the element voltages with the weights found from the inverse covariance matrix of interference signals is shown in equation 6.8.

$\mathbf{R}$ = covariance matrix of steering vectors of signals not of interest (SNOI)

w_o = steering vector for signal of interest (SOI)

$\mathbf{W}$ = combined null/beamforming weight

$\mathbf{E}$ = radiation pattern of individual elements

$\mathbf{Y}$ = total weighted sum of all element voltages

N = Number of antenna elements

$$\mathbf{W} = \mathbf{R}^{-1} w_o \tag{6.7}$$

$$\mathbf{Y} = \sum_{n=1}^{n=N} E(n)W(n) \tag{6.8}$$

The null-forming weights were produced with the inverse covariance matrix of interfering signal vectors. Digital synthesized null-forming is made from individual measurements with one element enabled at a time. Magnitude and phase for each element was exported and combined. The calculated weights were applied in post-processing. With analog measured null-forming, the calculated weights were applied to the PAC. Measurements were done with the eight elements enabled.

6.4 Null Weights Applied to the Simulated Array

The Covariance Matrix method was used to calculate null/beamforming weights and were applied to an 8 element simulated array. Equation 6.8 describes the method used. Figure 6.3 (a) shows a simulation with three jamming signals (i.e., SNOI) located at 60°, 75° and 120° with the desired signal being at broad side 90°. The simulation has good results for this scenario with each of the jamming SNOI having power of -20dB or less and the SOI having a power of -1dB. Figure 6.3 (b) shows a similar scenario with SNOI at 60°, 100° and 120° with the desired signal being at broad side 90°. The results show 0dB for the SOI which is desirable. For the three

SNOI the power is around -20dB which is desirable however the width of the null is very narrow which is not desirable. Figure 6.4 shows a different scenario with SNOI at 60° and 130° with the desired signal being not at broad side but shifted to 110°. The results show -3dB for the SOI which is not as desirable as broadside scenarios. For the two SNOI the power is around -20dB which is desirable.

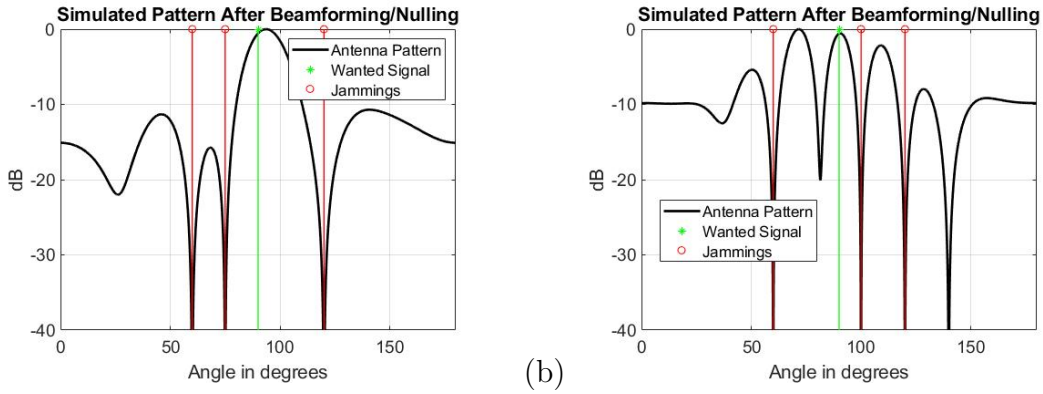

(a) (b)

Figure 6.3: Null-forming weights applied to a simulated 8-element antenna array (a) SOI at $\phi = 90°$ and SNOI at $\phi = 60°$, $\phi = 75°$ and $\phi = 120°$ (b) SOI at $\phi = 90°$ and SNOI at $\phi = 60°$, $\phi = 100°$ and $\phi = 120°$.

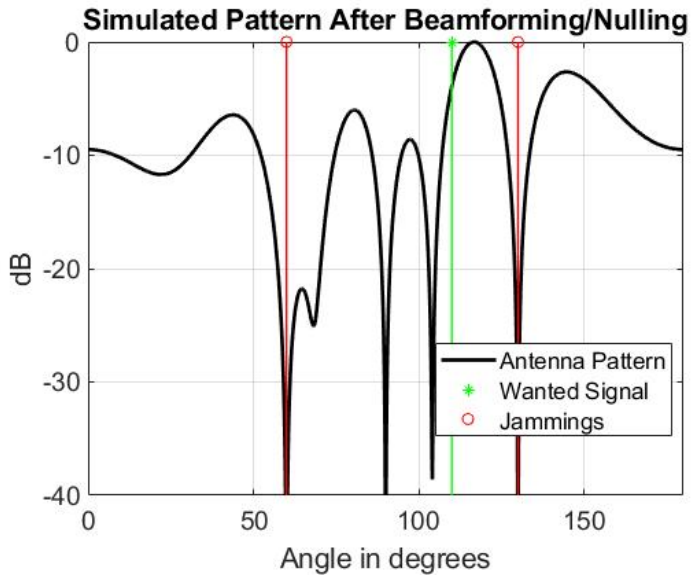

Figure 6.4: Null-forming weights applied to an 8-element antenna array with SOI at $\phi = 110^{\circ}$ and SNOI at $\phi = 60^{\circ}$ and $\phi = 130^{\circ}$.

Chapter 7

Laboratory Measurement Setup

7.1 Requirements of 3D Pattern Measurements of GPS Array Antenna

This section describes preferences for the process of GPS antenna measurement provided by the BAE Aerospace Company. We attempted to adhere to these preferences for taking measurements. We met the requirements in not all but some areas including providing a mounting ground for each antenna element, an anechoic chamber was used to block out of band interference, elements were spaced a half-wavelength apart, the response of each antenna element was recorded, antenna gain/magnitude was recorded in units of dB, phase was recorded in units of degrees, the RHCP response to linear polarized signals was recorded, the LP measurements were used to calculate the response to RHCP sources, and for the 3D measurements data was recorded in both the azimuth and elevation planes. The spatial resolution that is preferred by BAE is a measurement every four degrees in the azimuth plane from 0° to 360° and every two degrees in the elevation plane from 90° broadside to −20°. For the 3D measurements of the 1 by 6 GNNS array, a measurement was taken every two degrees from −90° to 90° for both the elevation and azimuth planes, where 0° is the antenna broadside. For the 3D measurements of the 7 element circular GNNS array,

a measurement was taken every five degrees from -90° to 90° for both the elevation and azimuth planes, where 0° is the antenna broadside. For the 2D measurement of S-Band 1 by 8 array, a measurement was taken every half degree from -90° to 90° for the elevation plane, where 0° is the antenna broadside.

7.2 Far-Field Anechoic Chamber

The NF and FF chambers both measure 3D radiation patterns. In the FF chamber, spherical mode was conducted using a positioner made in house that used a Velmex motor controller. This additional motor allowed the test antenna to be moved in elevation. Movement in azimuth was already possible with the built-in test stand in the chamber. The additional motor was used to enable the measurements FF 3D radiation patterns.

7.3 RHCP Pattern Measurements Using Linearly-Polarized Antennas

To acquire the measured radiation pattern of a circular polarized receiving antenna without access to a RHCP transmitting antenna, a linear transmit antenna can be used. Two linear measurements with orthogonal polarizaions can be taken of the electric field. The equation 2.1 defines this relationship. Measurements of a single element RHCP antenna was taken twice, using two orthogonal linear polarizations and then combined in post-processing with equation 2.1. The second measurement was with a RHCP TX antenna shown in Figure 3.1. The data from the two measurements are compared in Figure 7.1. As the comparison shows, the linear TX method and the RHCP TX method shows similar results which provides validation for the equation 2.1. The linear TX is shown is V-Pol polarization in Figure 7.2.

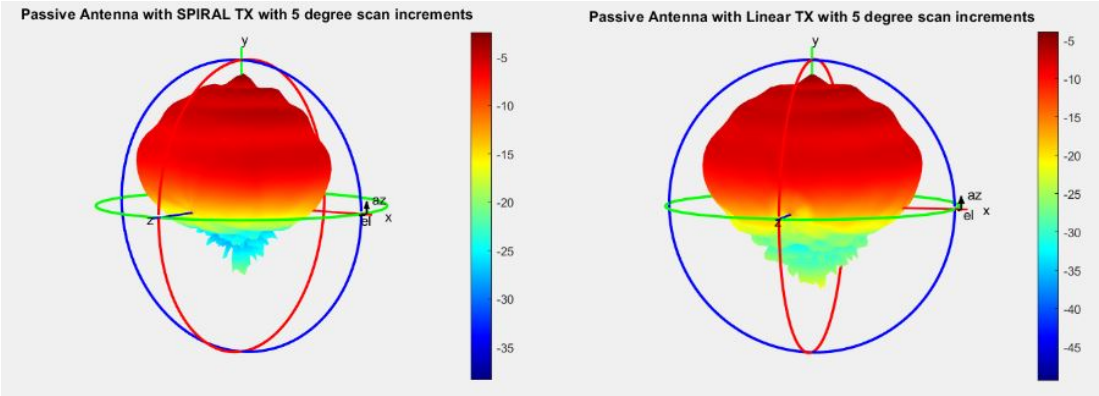

Figure 7.1: Comparison of Single Element 3D Pattern from RHCP TX and Linear TX Measurements.

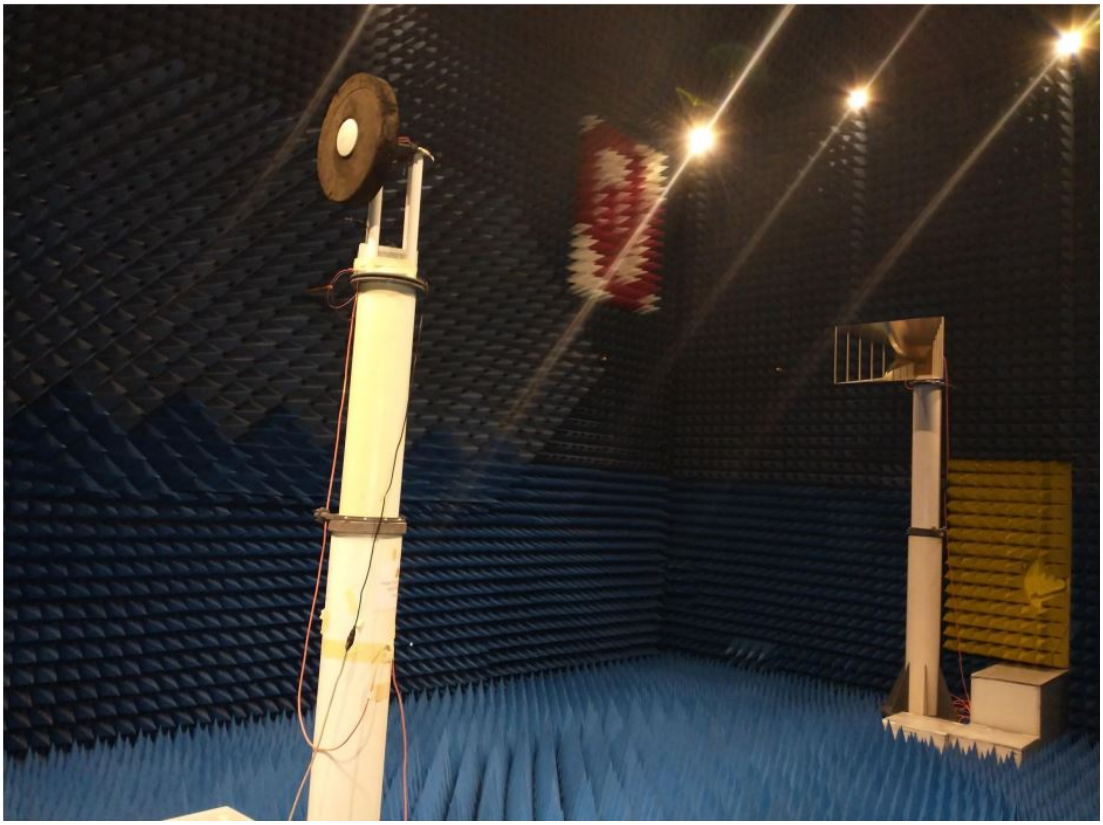

Figure 7.2: Linear TX antenna was used to measure an antenna in FF Chamber

7.4 NF Chamber Operating in Spherical Mode

The measurements were performed in a NF anechoic chamber using the spherical mode. All data has been recorded in the spherical coordinate system. The data measured has been for azimuth angles 180° to -180° and elevation angles -90° to 90°. For the elevation orientation, 0° is where incident normal of the test antenna is directly lined up with the transmit antenna.

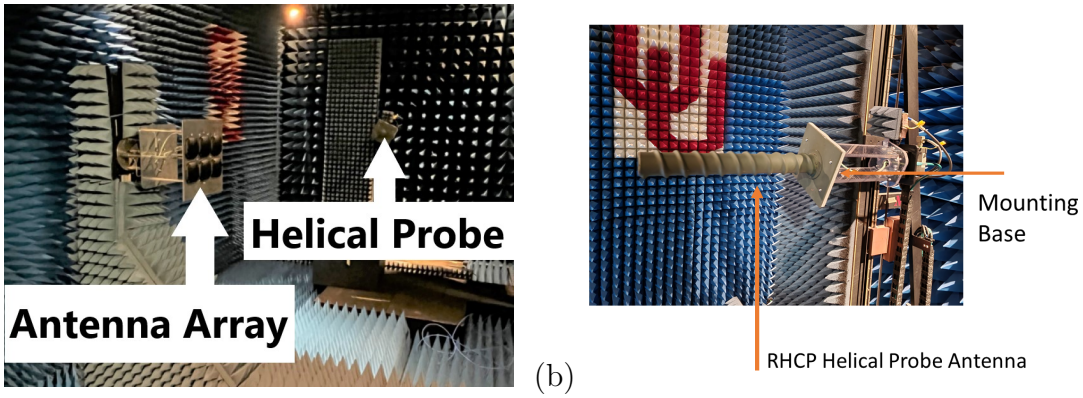

(a) (b)

Figure 7.3: NF chamber system measurement setup, (a) Spherical sampling positioning, (b) Mounting of helical probe antenna on the NF scanner.

7.5 NF Chamber Operating in X-Y Planar Mode

7.5.1 PAC Controller for the S-band Linear Array

The S-band linear array has been used in this study as a proof of the concept of the null-forming techniques. Although the S-band array does not operate in the GNSS frequency band and it operates in linear polarization instead of circular polarization, it is still a useful tool to verify the digital null-forming and steering algorithms. The array is attached to PAC modules that are interfaced with through a MATLAB program. With the PAC modules, we are able to change the phase and amplitude weights of each element. Phased Array Controllers are a form of analog beam-forming.

The PAC used has a 6-bit phase shifter and 6-bit attenuator. The 6-bit phase shifter was used to apply the null-forming weights. Figure 6.1 shows the required phase shift for each element in order to achieve a 30 degree shift of the main beam. Figure 6.2 shows the corresponding beam shift.

The equation for the phase shift of each element is shown below where θ is the scanning angle.

$$\beta = kdsin(\theta) \tag{7.1}$$

In the equation 7.5.1, θ is the steering angle in the elevation plane. The variable d is the distance between the center of the array to the individual elements on the x axis. The array is centered between the 4th and 5th elements which are the center elements. The distance from the probe to the array is 3λ.

Measurements were done in NF X-Y Planar scanning mode for an 8-element, S-band, dual-polarized linear antenna array (with V-pol being Co-Pol). The radiation patterns of the measured array were compared with the synthesized null-forming results.

Element	Phase Shift
1	0
2	270
3	180
4	90
5	0
6	270
7	180
8	90

Figure 7.4: Phase shift in degrees for 8-elements of the S-Band linear array. Required phase shift for each element in order to achieve a 30° shift of the main beam.

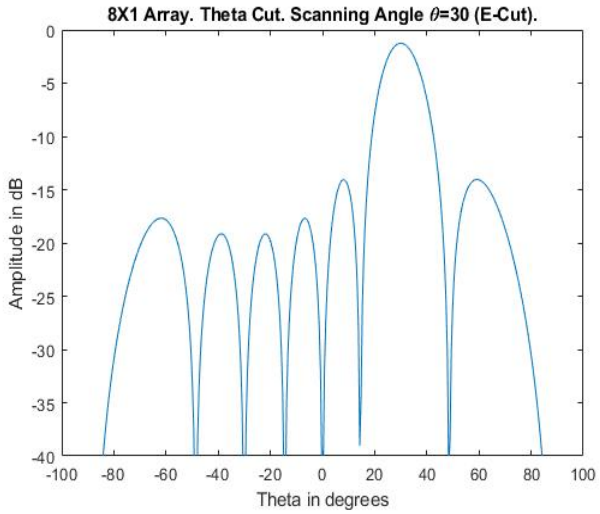

Figure 7.5: Theta cut with 30° phase shifting weight applied to each element.

(a) 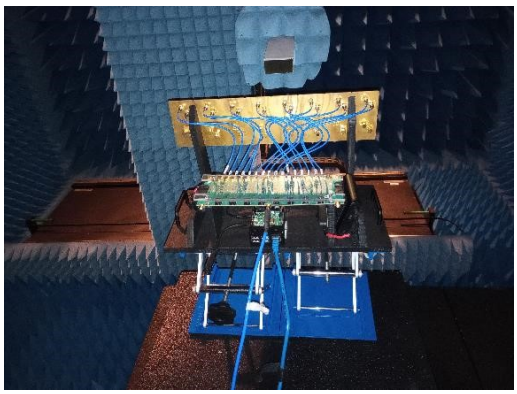 (b) 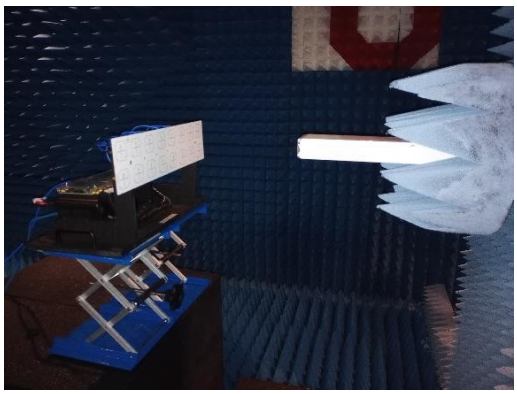

Figure 7.6: NF chamber X-Y planar mode setup, (a) PAC board attached to all 8 elements. (b) 8-element S-band array and waveguide TX probe.

(a) 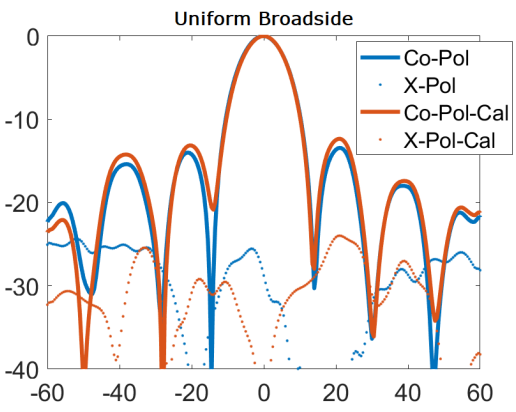

(b) 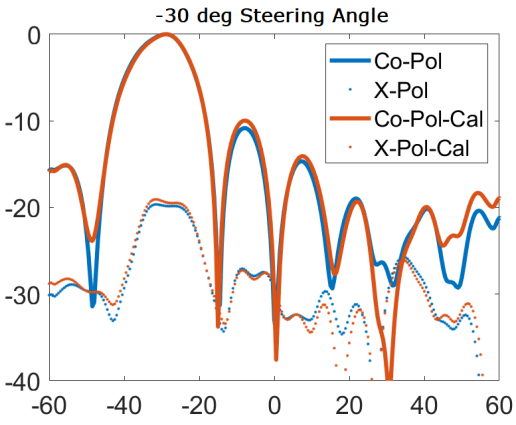

Figure 7.7: Comparison of Co-Pol and X-Pol radiation patterns of S-band 1 by 8 array, before and after calibration (a) Pattern with no steering applied and main lobe at 0° (broadside) (b) Pattern with $-30°$ steering applied.

7.5.2 RHCP Linear Array for GNSS Anti-jamming

Measurements were done in NF X-Y Planar scanning mode for the circular-polarized 6-element GNSS array in the NF range using the following configuration. The TX probe is aligned between the 3th and 4th elements which are the center elements. The distance from the probe to the array should be 3λ. All 6 elements were summed together with an analog power combiner before the data was digitized. The combined radiation patterns of the measured array were compared with the synthesized results in post-processing.

(a) 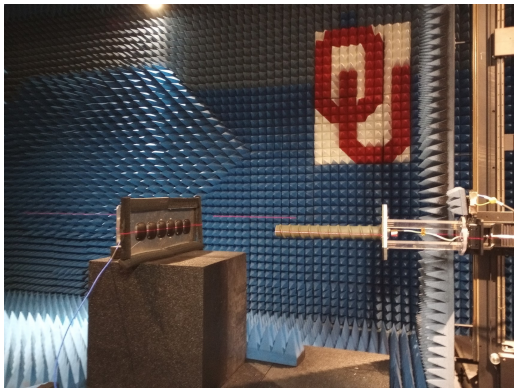 (b) 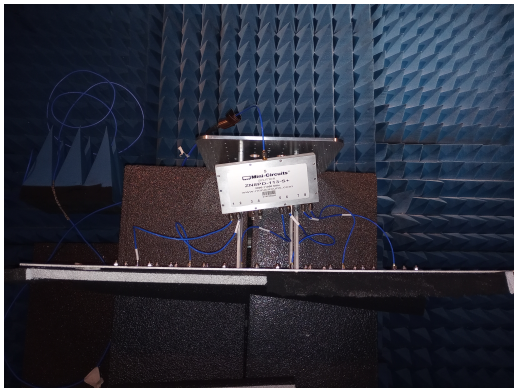

Figure 7.8: NF chamber X-Y planar mode setup, (a) 6-element GNSS ULA and helical TX probe (b) power combiner attached to all 6 elements.

7.6 Digitally Synthesized vs Analog-Beamformed Patterns

Both the six- element linear RHCP array and the eight-element S-band array were both measured and then the results were compared. The first way of measurement, referred to as the analog method, was having all elements active and measuring them all at once. The second way was with digital post-synthesis, where only one element was measured at a time, and the rest of the elements are match-terminated. Or, when

the PAC controller was used, the other elements could be disabled through the GUI interface.

The following are the steps for measurements with a power combiner. First, record one measurement with all array elements enabled at once. Then, export magnitude data which is in units of dB. Then, in post-processing normalize the data and then plot for analysis.

The following are the steps for digitally synthesized measurements. First, record individual measurements for each array element with only one element enabled at a time. Keep the TX probe aligned with the middle of the array elements for all scans. Next, export the phase and magnitude data from each element's measurement. Initially, from the VNA the magnitude is in units of dB and the phase in units degrees. In post-processing, phase is converted to radians and magnitude converted from dB to linear units. Then, the patterns of each element are calculated. To find the combined pattern of all array elements, weighted patterns from all elements are added together. After the calculations are made, the results are converted back to dB scale.

Chapter 8

Results and Discussion

8.1 3D Patterns of Single Patch Antenna

The examples of individual passive element patterns from NF measurements are shown in Figure 8.1. The measured patterns include amplitudes and are recorded in 3D spherical coordinates. The element amplitude patterns are consistent with expectations shown in the datasheet specifications. The pattern shows the desired characteristic of a patch antenna, such as the large beamwidth.

(a) 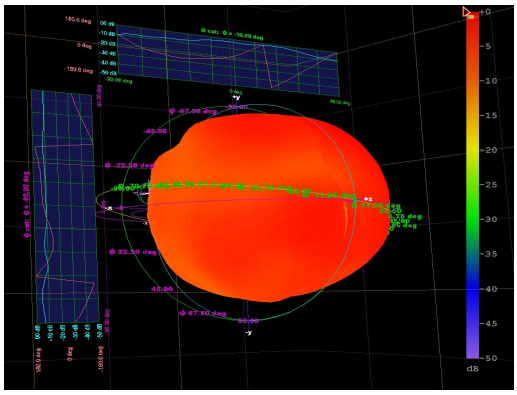 (b) 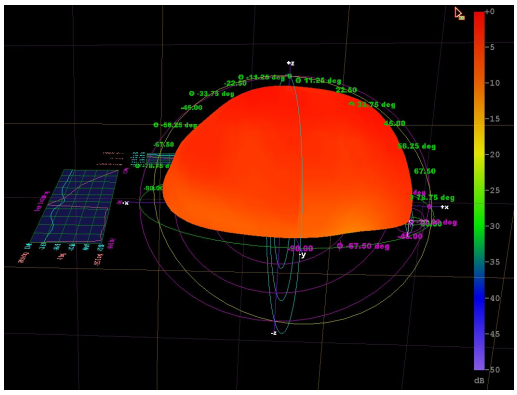

Figure 8.1: Pattern measurement of single element from near-field chamber, Spherical Mode measurement setup (a) top-view (b) side-view.

8.2 3D Pattern Synthesizing Based on the 1-by-6 Planar Array

This section summarizes the results of 3D pattern synthesis for 1.5 GHz GNSS array antenna, including the results for anti-jamming null forming. The NF chamber was used to perform 3D measurements of the passive element 1 by 6 array. Then post-processing was applied to create beam/null forming patterns. Neither the measured or synthesized measurements agree well with the expected and simulated results. Figure 8.2 (b) shows the expected simulated radiation pattern of the 6-element ULA. Figure 8.2 (a) shows the measured uniform pattern of the array with no weights applied. The expected pattern and the measured patterns do not show agreement. This error was thought to be caused in-part by edge effects. To combat EM interference from the edge of the ground plane, EM absorbing foam was attached to all four surrounding edges and measurements were taken again. Unfortunately, even with the EM absorbing foam, the errors persisted. To determine if the root of error was in the measurement processes or the antenna elements, both methods were compared. The measurement plot of Figure 8.2 (a) compares both the synthesized and power combined measurement processes. Both methods are compared to determine if the error can be isolated to the post-processing method or the hardware elements. Since both patterns show the same inaccuracies, it is assumed the error is not in either method of measurement. The error has been attributed to inaccuracies in the hardware of the elements. Even with the hardware error, figures 8.3 (c) and 8.3 (d) show that the beam was indeed able to shift but the uniform pattern was not aligned at zero degrees broadside as desired. With uniform weighting, the main lobe was resting at $\phi = 30°$. Figure 8.4 (a) and (b) show the results of applying null-forming weights to the 6-element GPS antenna array. With the hardware error of the elements, scenario shown in (a) shows at location of the SNOI there is a null of -7dB and at the SOI a

level of -3dB. For the scenario shown in (b), at locations of the SNOI there are nulls of -12dB and -7dB while at the SOI a level of -2dB.

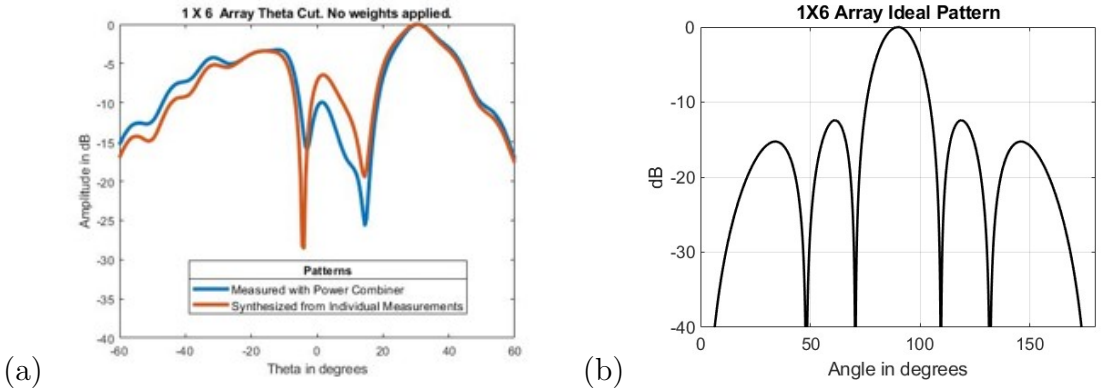

(a) (b)

Figure 8.2: Comparison between measured and ideal 1 X 6 arraypattern (a) Measured (b) Simulated.

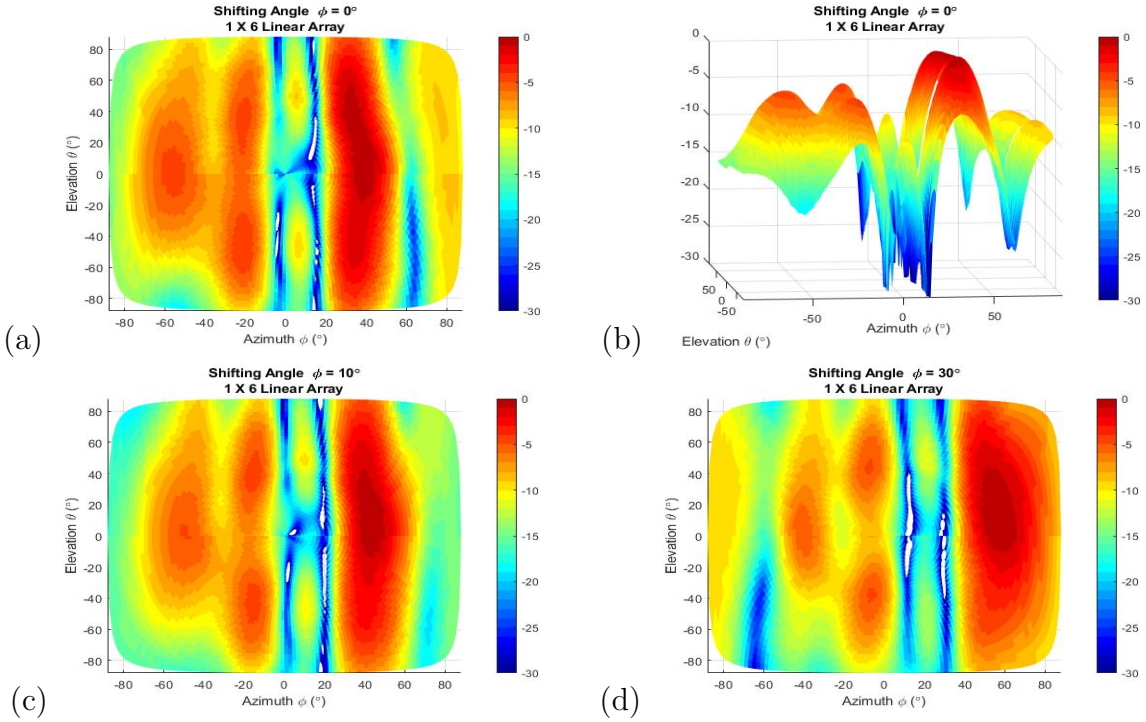

(a) (b) (c) (d)

Figure 8.3: Null steering and pattern synthesizing based on NF-measured active element data of the 6-element GPS antenna array. (a) and (b): 3D pattern from Uniform Weighting.(c) $\phi = 10°$ (d) $\phi = 30°$ Steering.

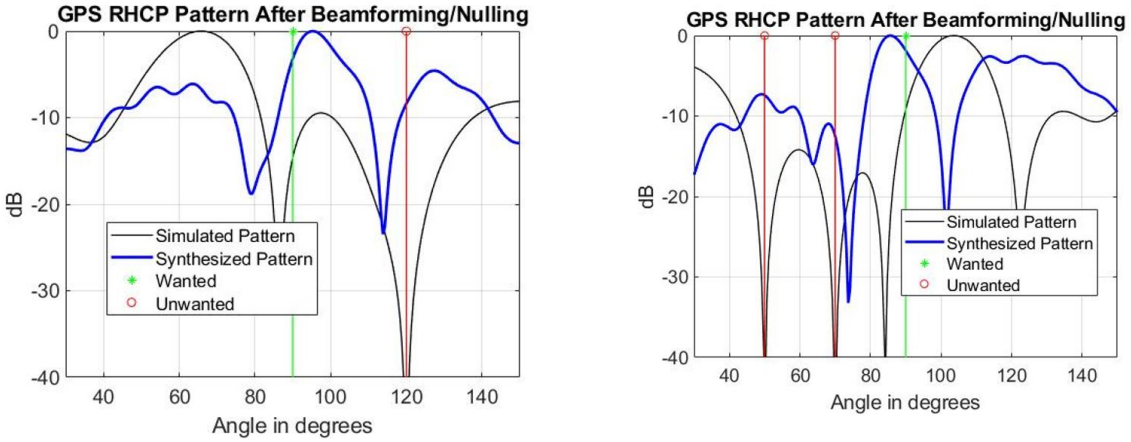

Figure 8.4: Null-forming weights applied to 6-element GPS antenna array with hardware defect. (a) SOI at $\phi = 90^\circ$ and SNOI at $\phi = 120^\circ$ (b) SOI at $\phi = 90^\circ$ and two SNOI at $\phi = 50^\circ$ and $\phi = 70^\circ$.

8.3 3D Pattern Synthesizing Based on the 2-by-3 Planar Array

The NF chamber was used to create 3D measurements of the passive element 2 by 3 array. Post-processing was then applied to generate the beam/null forming patterns. The 3D pattern of the array with uniform weighting is shown in Figure. 8.5 (a) and Figure. 8.5 (b). A 10° and then a 20° shift in the azimuth plane was applied in Figure. 8.5 (c) and Figure. 8.5 (d), respectively. The azimuth plane is along the axis with three elements linearly placed and the elevation plane is along the axis with 2 elements linearly placed. In the elevation plane, a 10° and then a 20° beam steering was applied in Figure. 8.5 (e) and Figure.8.5 (f). Weights were applied in the elevation and azimuth planes simultaneously (θ, ϕ) . Figure. 8.5 (g) shows the main beam steered to location (-10°, -20°). Figure. 8.5 (h) shows the main beam steered to location (10°, 20°).

The uniform pattern shown in Figure 8.5 (b) shows there is a Sidelobe Level (SLL) of -5db. This is undesirable as the expected SLL for a uniform array is -13dB. This error was thought to be caused in-part by edge effects. A test was enacted to determine if the error was indeed from edge effects. To combat possible EM interference from the edge of the ground plane, EM absorbing foam was attached to the ground plane of the 1 by 6 array and measurements were taken again. Unfortunately, even with the EM absorbing foam, errors persisted and the SLL was not desirable. With both the 1 by 6 array and the 2 by 3 array, the error has been attributed to inaccuracies in the hardware of the elements.

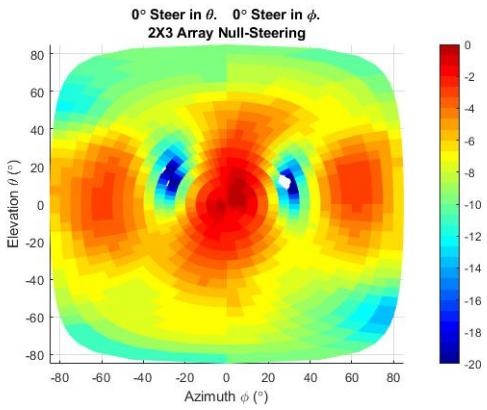
0° Steer in θ. 0° Steer in ϕ.
2X3 Array Null-Steering
Elevation θ (°)
Azimuth ϕ (°)

(a)

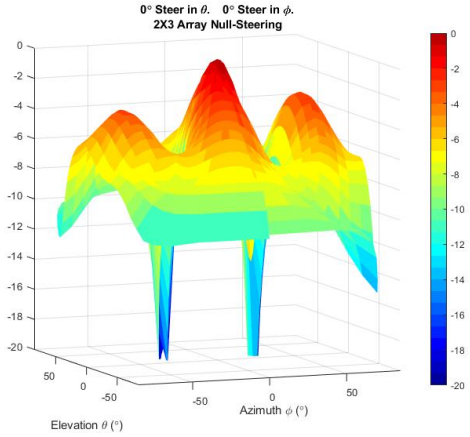
0° Steer in θ. 0° Steer in ϕ.
2X3 Array Null-Steering
Elevation θ (°)
Azimuth ϕ (°)

(b)

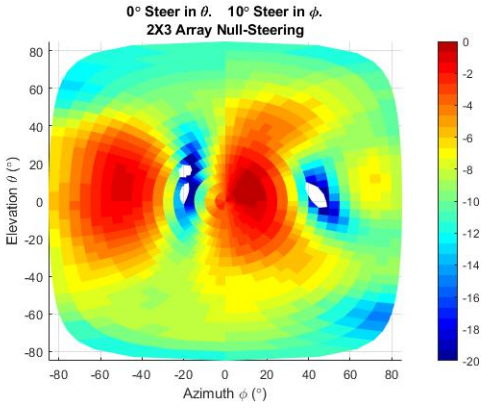
0° Steer in θ. 10° Steer in ϕ.
2X3 Array Null-Steering
Elevation θ (°)
Azimuth ϕ (°)

(c)

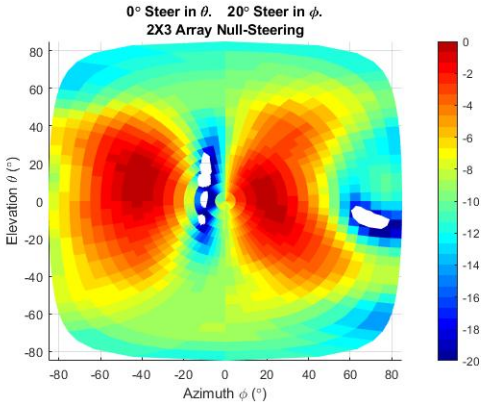
0° Steer in θ. 20° Steer in ϕ.
2X3 Array Null-Steering
Elevation θ (°)
Azimuth ϕ (°)

(d)

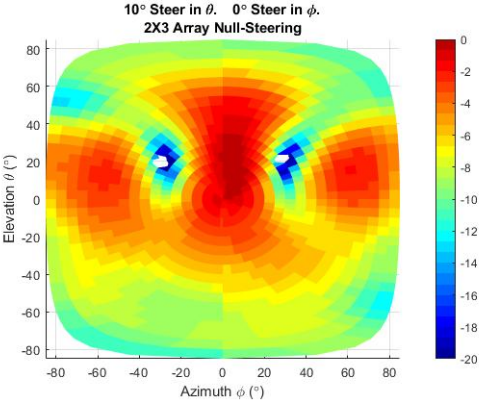
10° Steer in θ. 0° Steer in ϕ.
2X3 Array Null-Steering
Elevation θ (°)
Azimuth ϕ (°)

(f)

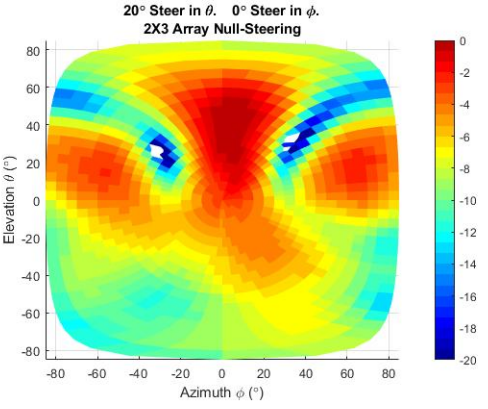
20° Steer in θ. 0° Steer in ϕ.
2X3 Array Null-Steering
Elevation θ (°)
Azimuth ϕ (°)

(g)

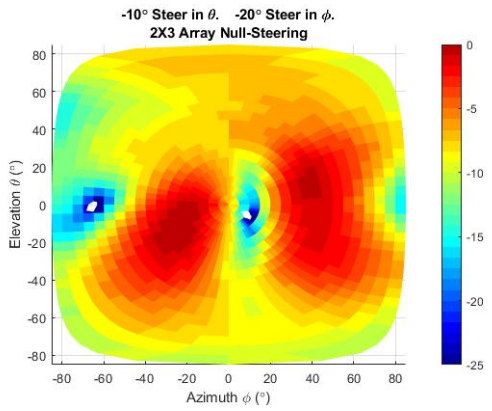

(h)

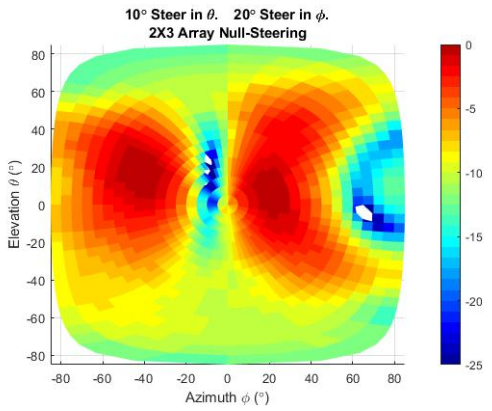

(i)

Figure 8.5: Null steering and pattern synthesizing based on NF-measured active element data of the 2 by 3 rectangular GPS antenna array. (a) and (b): 3D pattern from uniform weighting.(c) and (d): azimuth (ϕ) steering.(e) and (f): elevation (θ) steering. (g), (h) an (i): 3D patterns of steering to both elevation and azimuth angles/directions.

8.4 3D Pattern Synthesizing Based on 7-Element Circular Lattice Planar Array

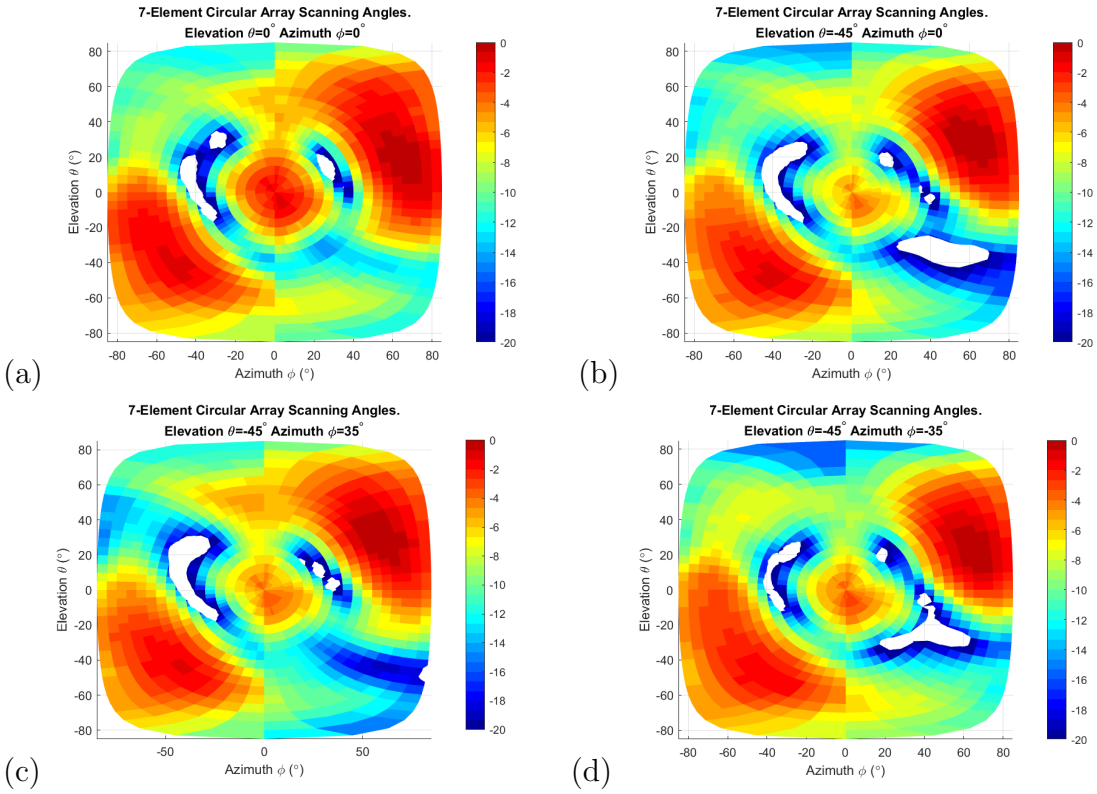

Figure 8.6: Null steering and pattern synthesizing based on NF-measured passive element data of the 7-element circular lattice GPS antenna array. (a) 3D pattern from Uniform Weighting (b): steering in elevation plane (c) and (d) Patterns of steering in both elevation and Azimuth angles/directions.

The NF chamber was used to create 3D measurements of the passive 7-element circular-lattice planar array. In post-processing, weights were applied for beam-forming purposes. The uniform pattern shown in Figure 8.6 (a) shows there is a high Side-Lobe-Level (SLL). This is undesirable as the expected SLL for a uniform array is -13 dB. This error was thought to be caused in-part by edge effects. A test was enacted to determine if the error was indeed from edge effects. To mitigate possible diffraction effects from the edge of the ground plane, EM absorbing foam was

attached to the ground plane of the 1 by 6 array and measurements were taken again. Unfortunately, even with the EM absorbing foam, errors persisted and the SLL was not ideal. With the 1 by 6 array, the 2 by 3 array, and the circular array, the error has been attributed to inaccuracies in the hardware of the elements.

8.5 Adaptive Null-Forming Results

8.5.1 Null Weights Applied to The Digitally Synthesized S-Band Array

Null/beamforming weights were calculated using the covariance matrix method and were digitally applied to an 8 element synthesized array in post-processing. Both the phase component and the amplitude co-efficient component of the complex weights were applied. The plots below compare the simulated array patterns to the measured patterns.

Table 8.1 combines the data for the level scenarios. The table shows the power level in dB at each of the locations of SNOI. The left column shows the location of the SOI for that specific scenario. At a null location, -20dB or less is desirable while 0dB is most desirable at the location of SOI.

Figure 8.7 (a) shows the adaptive response for a scenario with the SOI at broadside and two SNOI located at 75°, and 110°. The response shows a power level of 0dB for the SOI and power levels less than -20dB for both SNOI which is desirable.

Figure 8.7 (b) shows the adaptive response for a scenario with the SOI at broadside and two SNOI located at 110°, and 120°. The response shows a power level of 0dB for the SOI and power levels -20 dB and -18 dB for the SNOI.

With three nulls, Figure 8.8 (a) shows the adaptive response for a scenario with the SOI at broadside and three SNOI located at 60°, 75°, and 120°. The response shows a power level of 0dB for the SOI and power levels less than -20dB for both SNOI which

is desirable. For the three scenarios described above, the measured results show good agreement with the simulations.

Next, Figure 8.8 (b) shows a scenario where the SOI and the SNOI are all closely located within 10° of each other. The desired SOI shows a level of -4.5 dB and the SNOI shows -25 dB and -16 dB, respectively.

With four unwanted signals and the desired signal off of broadside, figure 8.9 (a) shows a scenario where the SOI is at 80° and the SNOI are at 60°, 100°, 120° and 140°. The desired SOI shows a level of -1dB and the SNOI shows less than -20dB for all four signals. Then, 8.9 (b) shows a scenario where the SOI is at 100° and the SNOI are at 60°, 80°, 120° and 140°. The desired SOI shows a level of -1dB and the SNOI show -18dB, -18dB, -30dB, and -35dB respectively.

With the SOI at 60°, Figure 8.12 (a) shows a scenario where the SNOI are located 75°, and 110°. The desired SOI shows a level of -1 dB and the SNOI shows -28 dB and -24 dB. Figure 8.12 (b) shows a scenario where the SNOI are located 110°, and 120°. The desired SOI shows a level of -1 dB and the SNOI shows -28 dB and -24 dB, respectively.

Eleven scenarios are presented each with different locations of SNOI. Six of the scenarios have two or more SNOI. Four cases have the location of the SOI at broadside and the rest of the location of the SOI off of broadside. The power levels at the locations of SNOI range from -14.5dB to -35dB. The results of the synthesized null-formations are summarized in table 8.1.

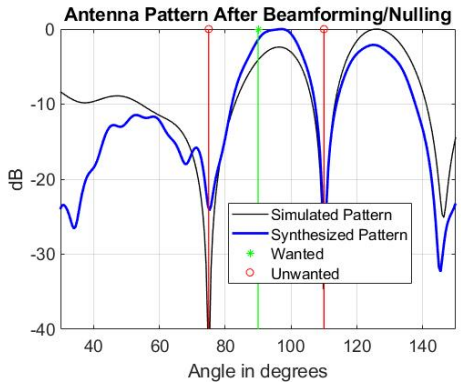

(a)

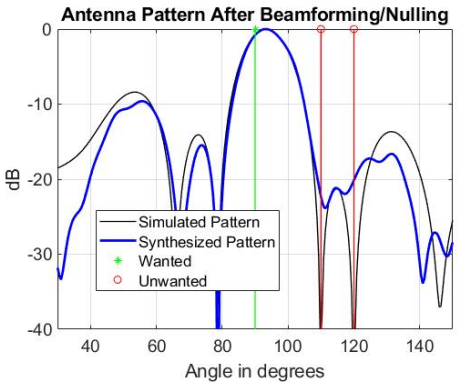

(b)

Figure 8.7: 3 GHz Array with Digital Null-forming(a) SNOI at 75° and 110°(b) SNOI at 110° and 120°.

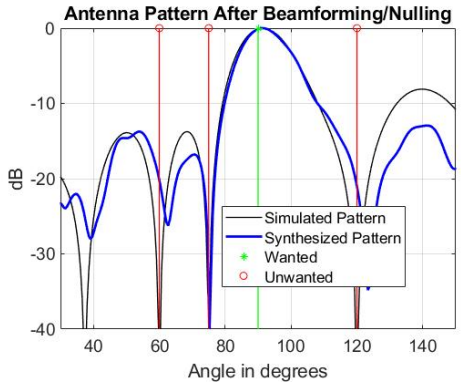

(a)

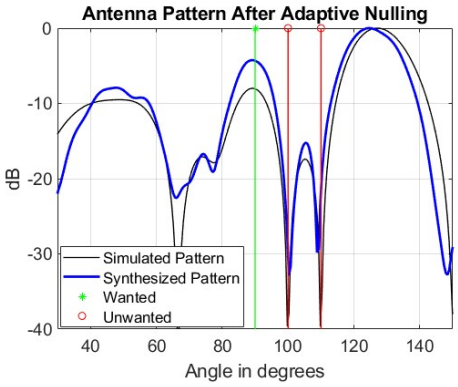

(b)

Figure 8.8: 3 GHz Array with Digital Null-forming(a) SNOI at 60°, 75° and 120° (b) SNOI at 100° and 100°.

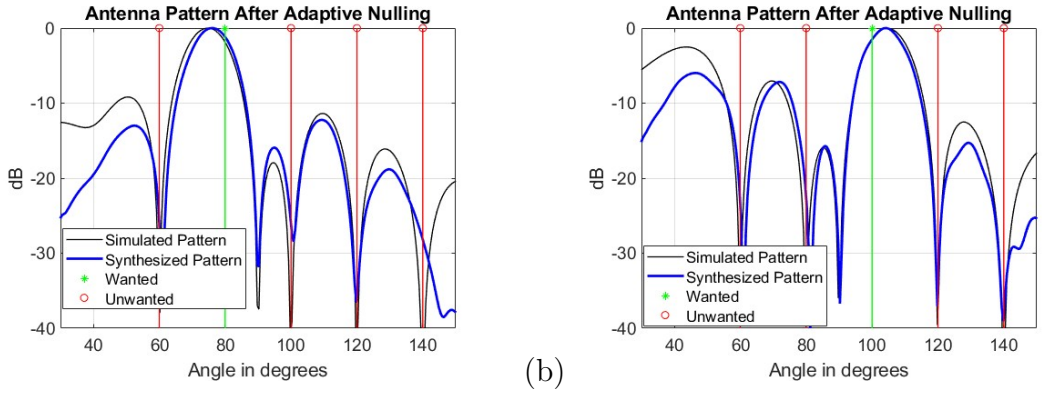

(a) (b)

Figure 8.9: SOI at 80° and 100° 3GHz Array with Digital Null-forming (a) SOI at 80°. SNOI at 60°, 100°, 120° and 140° (b) SOI at 100°. SNOI at 60°, 80°, 120° and 140°.

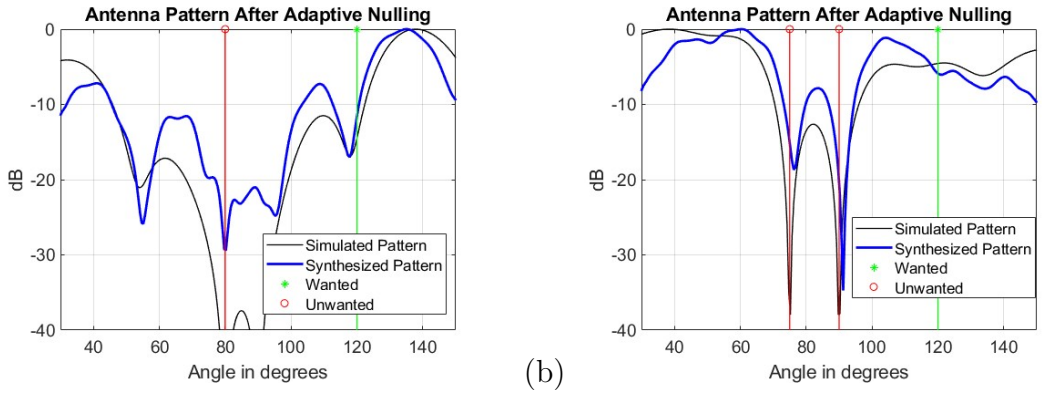

(a) (b)

Figure 8.10: SOI at 120° 3GHz Array with Digital Null-forming (a) SNOI at 80° (b) SNOI at 75°, 90°.

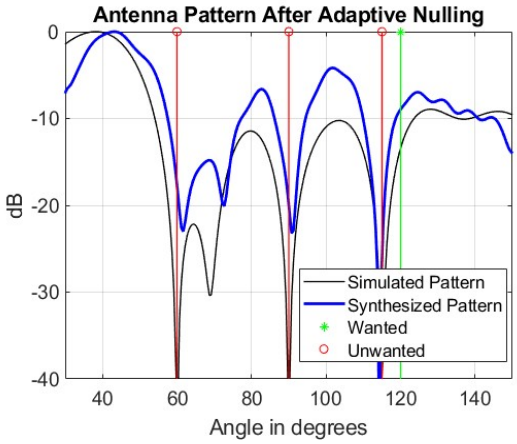

Figure 8.11: SOI at 120° 3GHz Array with Digital Null-forming (a) SNOI at 60°, 90°, and 115°.

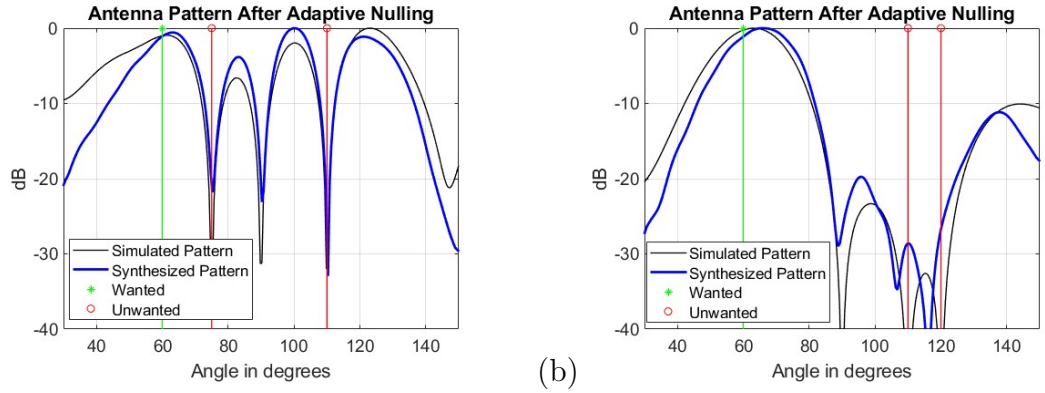

(a) (b)

Figure 8.12: Synthesized Digital Null-forming with SOI at 60° instead of broadside (90°) for S-band Array (a) SNOI at 75° and 110° (b) SNOI at 110° and 120°.

Table 8.1: Null-Depths of Synthesized Array Patterns at the Directions of Signals-Not-of-Interest (SNOI) As Outputs of Digital Null-Forming. Eleven Different Scenarios.

		SNOI								
	SOI	60°	75°	80°	90°	100°	110°	115°	120°	140°
1.	90°			-23dB		-20dB				
2.	90°					-20dB	-18dB			
3.	90°		-18dB	-23dB			-20dB			
4.	90°					-25dB		-15dB		
5.	80°		-28dB		-23dB			-35dB	-28dB	
6.	100°	-18dB		-18dB					-29dB	-35dB
7.	120°		-26dB							
8.	120°		-13dB		-15dB					
9.	120°	-16dB			-20dB			-18dB		
10.	60°		-18dB				-18dB			
11.	60°							-29dB	-25dB	

8.5.2 Null Weights Applied to the Analog Hardware of the S-Band Array

Measurements were done in NF X-Y Planar mode for the 8-element S-band (3 GHz) array (with V-pol being Co-Pol). Null/beam-forming weights were calculated using the Covariance Matrix method. The complex weights applied to the analog hardware included the phase component but not the amplitude co-efficient component. The complex weights were applied via the 6-bit phase shifter of a phased array controller for an 8-element array. The plots below compare the simulated array patterns, the

digitally synthesised patterns, and the measured analog patterns (which are shown in red). Figure 8.13 shows scenarios with the SOI at broadside and Figure 8.14 shows scenarios where the desired signal is not at broadside.

Table 8.2 combines the data for various scenarios. The table shows the power level in dB at each of the locations of SNOI. The left column shows the location of the SOI for that specific scenario. At a null location, -20dB or less is desirable while 0dB is most desirable at the location of SOI.

Figure 8.13 (a) shows the adaptive response for a scenario with the SOI at broadside and two SNOI located at 110° and 120°. The response shows a power level of 0dB for the SOI and power levels -20 dB and -18 dB for the SNOI.

Figure 8.13 (b) shows the adaptive response for a scenario with the SOI at broadside and two SNOI located at 75° and 110°. The response shows a power level of 0dB for the SOI and power levels -18dB and -11 dB for the SNOI.

With three jamming signals, Figure 8.13 (c) shows the adaptive response for a scenario with the SOI at broadside and three SNOI located at 60°, 75°, and 110°. The response shows a power level of 0 dB for the SOI and power levels -20dB, -15dB and -18dB for the signals not of interest.

Figure 8.13 (d) shows the adaptive response for a scenario with the SOI at broadside and two SNOI located at 100° and 110°. The response shows a power level of 0dB for the SOI and power levels -18 dB and -9dB for the SNOI. For this case, there is not good agreement between the outputs of the digital (blue) and analog (red) methods. The digital methods produced more desirable results. For example the SNOI have power levels at -30dB or less.

Figure 8.14 (a) shows the adaptive null-forming response for a scenario with the SOI at 60° and two SNOI located at 90°, and 100°. The response shows a power level of -3dB for the SOI and power levels -8 dB and -11 dB for the SNOI.

Figure 8.14 (b) shows the adaptive algorithm response for a scenario with the SOI at 60° and two SNOI located at 90° and 100°. The response shows a power level of -0dB for the SOI and power levels -8 dB and -14 dB for the SNOI.

Figure 8.14 (c) shows the adaptive algorithm response for a scenario with the SOI at 60° and one SNOI located at 90°, and 100°. The response shows a power level of -3dB for the SOI and power level of -12 dB for the SNOI.

Seven scenarios are presented with different directions of SNOI. Six of the scenarios have two or more SNOI sources. Four cases have the location of the SOI at broadside and three cases have the SOI 30° off broadside. The null depths at the locations of SNOI range from -8dB to -25dB. The results of the analog null-formations are summarized in table 8.2.

Table 8.2: Null-Depths of Array Patterns at the Directions of Signals-Not-of-Interest (SNOI) from Analog Null-Forming. Seven Different Scenarios.

						SNOI				
	SOI	60°	75°	80°	90°	100°	110°	115°	120°	140°
1.	90°						-25dB		-24dB	
2.	90°		-16dB				-11dB			
3.	90°	-19dB	-14dB						-17dB	
4.	90°					-18dB	-9dB			
5.	60°				-8dB	-12dB				
6.	60°				-7.5dB				-14dB	
7.	60°					-12dB				

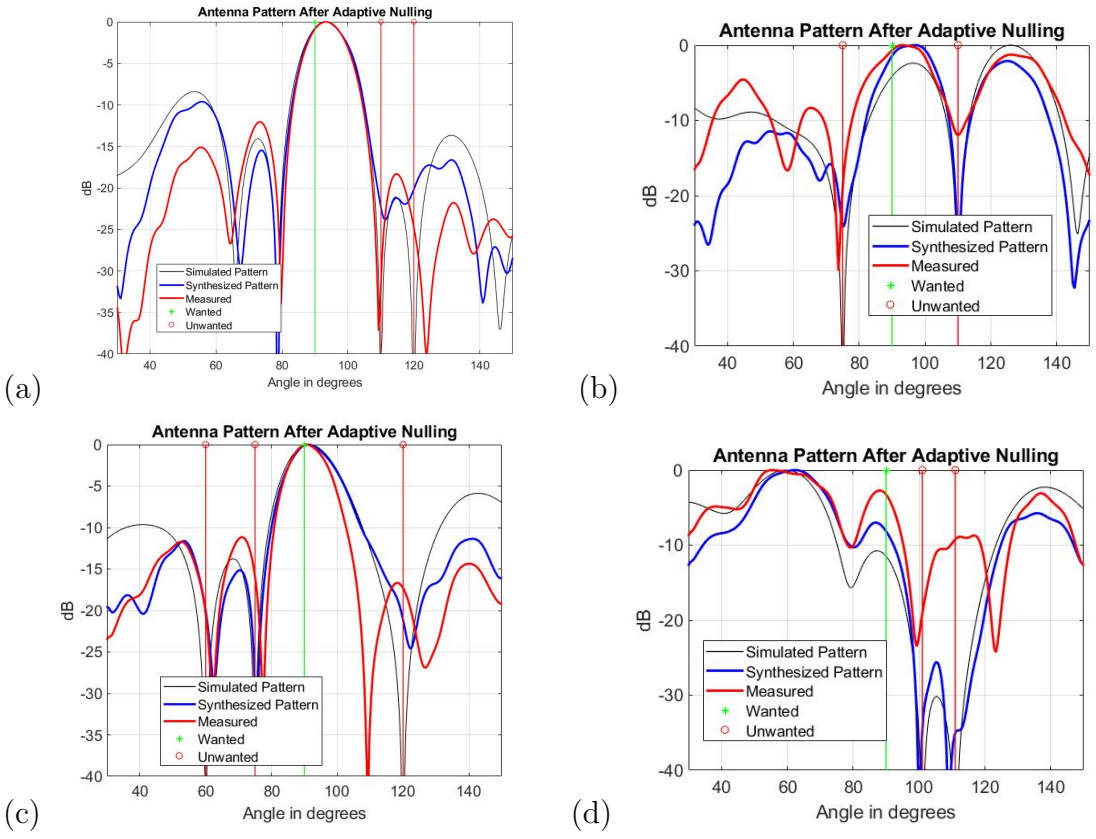

Figure 8.13: Null-forming of the S-band array Using the PAC Controller (a) SNOI located at 110°, and 120° (b) SNOI located at 75°, and 110°, (c) SNOI located at 60°, 75°, and 120°. (d) SNOI located at 100°, and 110°, respectively.

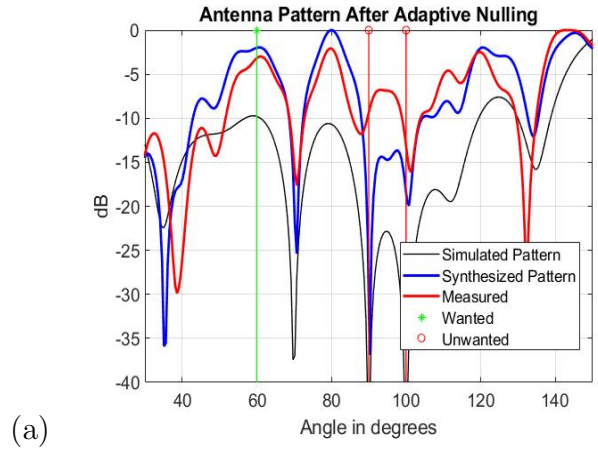

(a)

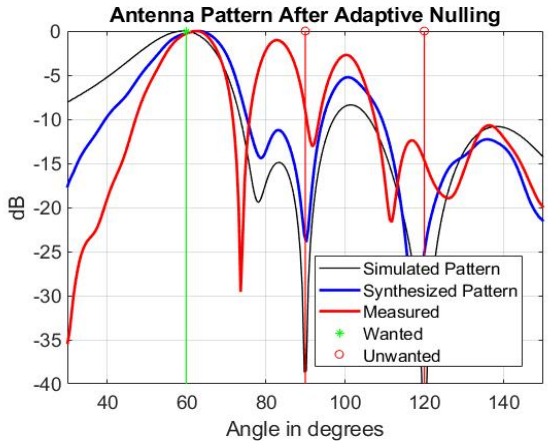

(b)

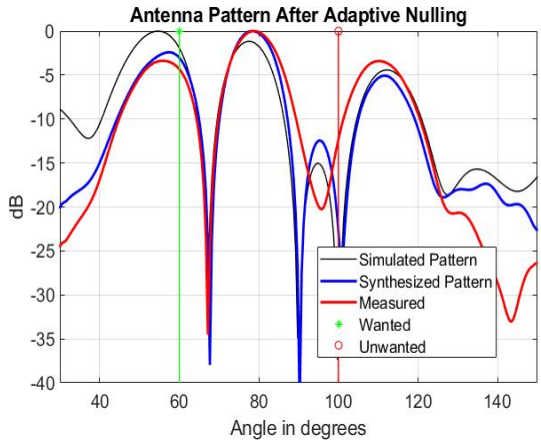

(c)

Figure 8.14: S-band Array Null-forming with Analog PAC Controller SOI at 60° (a) SNOI located at 110°, and 120° (b) SNOI located at 75°, and 110°(c) SNOI located at 60°, 75°, and 120°.

8.6 Optimization of Null Forming Algorithm

There are multiple ways of optimization for the beam-forming and null-forming algorithms, including gradient descent algorithm, using the cost function and solving for the minimum parameters, or least squares curve fitting to name a few. A likely approach to the optimization of the null-forming methods is the use of a genetic algorithm to find the minimizing parameters of the cost function that is made from the ideal and the practical radiation patterns.

The goal of this approach would be to minimize the absolute value difference between the ideal simulation and the practical measurements. A MATLAB solver would be used with the cost function of the practical and simulated data. The values that the solver converges to are the weights that are needed for the minimization of the cost function. These weights would then be the optimization weights for the antenna elements (Vats 2020). The genetic algorithm would likely be the solver chosen to solve for the minimizing parameters of the cost function. (Kolworks 2003, Mathworks 2023b, Biswas 2022, Atzemourt et al. 2022 and Vats 2020)

$$J(b) = \sum_{x=1}^{\mathrm{X}} |\mathbf{E}(x)_{simulated} \ - \ b \times \ \mathbf{E}(x)_{practical}| \tag{8.1}$$

The cost function is shown as J in equation 8.1 where X is the number of data points in measurement of the radiation pattern ($\mathbf{E}$). For example, if a measurement was take every two degrees from -90° to 90°, the number of data points would be ninety which would make $X = 90$. The variable $\mathbf{E}(x)_{practical}$ represents the data from the practical measurements and $\mathbf{E}(x)_{simulated}$ represents the ideal data from applying the calculated null-forming weights to a simulated array pattern produced from the geometry of the array. The variable b is the minimizing parameter. The value of b that the solver converges to becomes the optimizing beam-forming weight that is to be applied to $\mathbf{E}(x)_{practical}$ in order to produce an optimized pattern. (Vats 2020)

Chapter 9

Conclusion and Future Work

9.1 Summary of Contributions

In summary, this thesis achieved the investigation results and improvements in the following areas: To begin, 3D-characterization of GNSS antenna and array radiation patterns have been measured, and the data has been presented for anti-jamming and anti-interference array design and analysis. Then, adaptive null-forming based on the digital beamforming techniques were applied. Performance was evaluated based on how well the nulls were able to attenuate the unwanted interference while still having the main beam directed toward the desired signal. Lastly, comparison of analog and digital beam-forming results using customized anti-jamming array hardware, was summarized.

The first chapter introduced the challenges of GPS signal reception and the application of null-forming arrays for the FAA's GNSS operation missions.

The second chapter gave background information on GNSS and then gave characteristics of GNSS antennas, and discussed circular polarization and transmission with both helical and linear transmit antennas. Then an evaluation was presented on passive patch antennas.

The third chapter gave an overview of the antenna elements used in this study including the helical antenna, rectangular wave-guide antenna, as well as the made-in-house and commercial-off-the-shelf patch GPS antennas. It also discussed the multiple array layouts used in this study including the 1 by 6 linear L1-band array, the 2 by 6 rectangular L1-band array, the 7-element circular L1-band array and the 1 by 8 S-band reference array.

The fourth chapter discussed the models regarding linear and planar phased arrays. The conventional beam-forming algorithm and the array factor were explained. The differences between digital and analog beamformers were discussed and examples were given in chapter five.

Chapter six examined null-forming techniques. The side-lobe canceler method was explained and preliminary results were shown. The Covariance Method was then explained and simulated results were shown. The calculated weights were applied to a simulated array. The simulated Covariance method created null depths of -18dB to -30dB. The simulation showed scenarios with three SNOI sources.

Chapter seven discussed the laboratory measurement setups for the Far-field Anechoic Chamber and the Near-field Anechoic chamber. Near Field, Spherical, and X-Y planar modes were discussed. The set-up for the L1-band RHCP and S-band H-V-Pol arrays have been explained. The PAC controller for the S-band array was discussed and the differences between digitally synthesized and analog beam-formed patterns was discussed.

Chapter eight showed the measured 3D radiation patterns for a single patch antenna, 1 by 6 linear array, 2 by 3 planar array and the 7-element circular planar array. Beam-forming weights were applied in post-processing and the results showed error that has been attributed to hardware error of the antenna elements. The digitally synthesized 2D radiation patterns of the 1 by 8 S-band array was shown with the

applied null-forming weights calculated from the covariance matrix method. The results from eleven different scenarios are shown. The scenarios include five different elevation angle locations of the SOI along with 2-4 SNOI sources simultaneously. The applied weights created nulls in the synthesized patterns. The null depths ranged from -14dB to -30dB. The analog 2D radiation patterns of the 1 by 8 S-band array was shown with the applied null-forming weights calculated from the covariance matrix method. The data from seven different scenarios are shown with different directions of SNOI. Six of the scenarios have two or more SNOI sources. Four cases have the location of the SOI at broadside and three cases have the SOI 30° off broadside. The applied weights created nulls in the measured analog patterns. The null depths at the locations of SNOI ranged from -8dB to -25dB. Null-forming weights were adaptively calculated from the known directions of SNOI and SOI via the Covariance Matrix method. The weights were applied to a synthesized array in post-processing. The weights were also applied to the same array through an analog PAC. The results of the synthesized and analog method were compared. The digitally synthesized patterns had deeper null-depths than that of the analog patterns. Compared to the analog method, the digitally-synthesized patterns performed closer to the ideal simulated radiation patterns of null-formations. Differences between the synthesized and measured results may be attributed to the following reasons. For digital synthesis the phase component and the amplitude co-efficient component of the complex weights were both applied. Unlike the analog PAC boards where only the phase component of the complex weight was applied. The differences in the analog results also may be due to any losses and/or inaccuracies in the cables and hardware setup that are not present in digital synthesis. These hardware losses and inaccuracies could be opposed with further calibration of the array and PAC setup. With complete calibration of the PAC hardware, the analog results would likely emulate that of the synthesized results.

9.2 Future Work

Regarding the system hardware, future work may include the development of phase and amplitude control modules for GNSS antenna array with circular polarization. Regarding post-processing techniques, future works may include the optimization of the null-forming method by using more advanced algorithms, such as genetic algorithm, to find the minimizing parameters of the cost function that is based on the difference between simulated and measured radiation patterns. Also, there has been research done on utilizing Deep Learning, for fast adaptive beamforming, which was published in an IEEE paper Kim et al. (2022). This method uses the Capon method for training a neural network. Future works could include the application of similar machine learning and/or deep learning methods applied to GNNS antennas for adaptive null-forming.

Bibliography

Atzemourt, M., Z. Hachkar, Y. Chihab, and A. Farchi, 2022: Beamforming optimization by binary genetic algorithm. *2022 8th International Conference on Optimization and Applications (ICOA)*, 1–5, doi:10.1109/ICOA55659.2022.9934485.

Balanis, C. A., 2005: *Antenna Theory Analysis and Design*. Wiley.

Benedicto, J., S. Dinwiddy, G. Gatti, R. Lucas, and M. Lugert, 2000: Galileo: Satellite system design. *European Space Agency*, Int. Business.

Biswas, P., 2022: Genetic algorithm — an optimization approach. *Towards Data Science*.

Bose, A., S. Khobahi, and M. Soltanalian, 2021: Efficient waveform covariance matrix design and antenna selection for mimo radar. *Signal Processing*, **183**, 107 985, doi:https://doi.org/10.1016/j.sigpro.2021.107985, URL `https://www.sciencedirect.com/science/article/pii/S0165168421000244`.

Brachvogel, M., M. Niestroj, S. Zorn, M. Meurer, S. N. Hasnain, R. Stephan, and M. A. Hein, 2020: A new array concept using spatially distributed subarrays for unambiguous gnss interference mitigation in automotive applications. *NAVIGATION*, **67 (1)**, 23–41, doi:https://doi.org/10.1002/navi.353, URL `https://onlinelibrary.wiley.com/doi/abs/10.1002/navi.353`, `https://onlinelibrary.wiley.com/doi/pdf/10.1002/navi.353`.

Cheng, D. K., 1989: Field and wave electromagnetics. *Field and Wave Electromagnetics*, Addison Wesley, Inc.

Cuesll, 2023: Covariance matrix. URL `https://www.cuesllc.com/algebra/covariance-matrix/`, URL `https://www.cuesllc.com/algebra/covariance-matrix/`.

Delos, B. K. J., P. Broughton, 2020: Phased array antenna patterns—part 1: Linear array beam characteristics and array factor. **54**.

Dovis, F., 2015: *GNSS Interference Threats and Countermeasures*. Artech House.

EMViso, 2021a: Defining the array factor — lesson 2. URL `https://www.youtube.com/watch?v=wfN3MmjPz6k&t=166s`, URL `https://www.youtube.com/watch?v=wfN3MmjPz6k&t=166s`.

EMViso, 2021b: Uniform antenna arrays — lesson 3. URL https://www.youtube.com/watch?v=ReD2cB7EhWo, URL https://www.youtube.com/watch?v=ReD2cB7EhWo.

FAA, 2023: Satellite navigation - gbas - how it works. URL https://www.faa.gov/about/office_org/headquarters_offices/ato/service_units/techops/navservices/gnss/laas/howitworks, URL https://www.faa.gov/about/office_org/headquarters_offices/ato/service_units/techops/navservices/gnss/laas/howitworks.

Fairclough, C., 2017: Designing a butler matrix beamforming network with rf modeling. *COSMOL*.

Gondy, W. J. F., David, 2002: Design of a hybrid and flexible height reference system for flight inspection. *Proceedings of the 15th International Technical Meeting of the Satellite Division of The Institute of Navigation (ION GPS 2002)*, 2388–2395.

GPS.gov, 2022: Augmentation systems. URL https://www.gps.gov/systems/augmentations/, URL https://www.gps.gov/systems/augmentations/.

Gregory, M. D., Z. Bayraktar, and D. H. Werner, 2011: Fast optimization of electromagnetic design problems using the covariance matrix adaptation evolutionary strategy. *IEEE Transactions on Antennas and Propagation*, **59 (4)**, 1275–1285, doi:10.1109/TAP.2011.2109350.

Hofmann-Wellenhof, B., H. Lichtenegger, and E. Wasle, 2007: *GNSS–global navigation satellite systems: GPS, GLONASS, Galileo, and more*. Springer Science & Business Media.

Kim, Y., D. Schvartzman, R. D. Palmer, and T.-Y. Yu, 2022: Fast adaptive beamforming using deep learning for digital phased array radars. *2022 IEEE International Symposium on Phased Array Systems Technology (PAST)*, 01–07, doi:10.1109/PAST49659.2022.9975038.

Kolman, D. R., B. Hill, 2008: *Elementary Linear Algebra with Applications*. Pearson Prentice Hall.

Kolworks, 2003: *Appendix II: MATLAB Code*, 211–232. John Wiley Sons, Ltd, doi:https://doi.org/10.1002/0471671746.app2, URL https://onlinelibrary.wiley.com/doi/abs/10.1002/0471671746.app2.

Kraus, R. F. E. B., T., 2014: Use of the signal polarization for anti-jamming and anti-spoofing with a single antenna. *Proceedings of the 27th International Technical Meeting of the Satellite Division of The Institute of Navigation (ION GNSS+ 2014)*, 3495–3501.

Kumar, A., S. Kumar, P. Lal, P. Saikia, P. K. Srivastava, and G. P. Petropoulos, 2021: Chapter 1 - introduction to gps/gnss technology. *GPS and GNSS*

Technology in Geosciences, G. p. Petropoulos and P. K. Srivastava, Eds., Elsevier, 3–20, doi:https://doi.org/10.1016/B978-0-12-818617-6.00001-9, URL https://www.sciencedirect.com/science/article/pii/B9780128186176000019.

La Valle, R. L., J. G. García, and P. A. Roncagliolo, 2019: Antenna coupling and out of band interference effects on a high precision gnss receiver. *2019 Argentine Conference on Electronics (CAE)*, 47–51, doi:10.1109/CAE.2019.8709271.

Langley, R. B., 1998: A primer on gps antennas. *GPS World*.

Lopez La Valle, J. R. P., Ramon Garcia, 2019: Antenna coupling and out of band interference effects on a high precision gnss receiver.

Maloney, J. A., 2020: Anti-jam gps controlled reception pattern antennas for man-portable applications. *Doctoral Dissertations*, doi:https://doi.org/10.7275/15998807.

Mathworks, 2023a: Array pattern synthesis part i: Nulling, windowing, and thinning. URL https://www.sllcworks.com/help/phased/ug/array-pattern-synthesis.html, URL https://www.sllcworks.com/help/phased/ug/array-pattern-synthesis.html.

Mathworks, 2023b: Genetic algorithm. URL https://www.mathworks.com/help/gads/genetic-algorithm.html, URL https://www.mathworks.com/help/gads/genetic-algorithm.html.

Monteiro, S. N. H. V., 2015: Improved null steering with sidelobe canceller for linear antenna arrays. *International Journal of Advanced Research in Computer and Communication Engineering*, **4**.

Montenbruck, O., A. Hauschild, P. Steigenberger, U. Hugentobler, P. Teunissen, and S. Nakamura, 2013: Initial assessment of the compass/beidou-2 regional navigation satellite system. *GPS solutions*, **17**, 211–222.

Priyanka, P. and O. Vishnu, 2011: Sidelobe canceller system for phased array radar. *2011 12th International Radar Symposium (IRS)*, 855–862.

Rao, W. F. R. M. K., R. B. Kunysz, 2012: *GPS/GNSS Antennas. GNSS Technology and Application Series*. Artech House.

S. Kim, Y. L., S. Yoon and H. Shin, 2019: A miniaturized butler matrix based switched beamforming antenna system in a two-layer hybrid stackup substrate for 5g applications. **8**, 1232.

Salazar, D. J., 2022: Ece 5973 phased array antenna lecture series. University of Oklahoma.

Shelley, S., J. Costantine, C. Christodoulou, D. Anagnostou, and J. Lyke, 2010: Fpga-controlled switch-reconfigured antenna. *Antennas and Wireless Propagation Letters, IEEE*, **9**, 355 – 358, doi:10.1109/LAWP.2010.2048550.

Skolnik, M. L., 2001: *Introduction to Radar Systems*. McGraw Hill.

Van Trees, H., 2002: *Adaptive Beamformers*, chap. 7, 710–916. John Wiley Sons, Ltd, doi:https://doi.org/10.1002/0471221104.ch7, URL https://onlinelibrary.wiley.com/doi/abs/10.1002/0471221104.ch7, https://onlinelibrary.wiley.com/doi/pdf/10.1002/0471221104.ch7.

Vats, P., 2020: Linear regression, cost function and gradient descent algorithm..clearly explained !! URL https://www.youtube.com/watch?v=erfeZg27B7A, URL https://www.youtube.com/watch?v=erfeZg27B7A.

Wen, G., Y. Huang, H. Yuan, B. Tang, and H. Zhang, 2022: Design and realization of small anti-jamming gnss antenna based on ltcc. *Proceedings of the 3rd International Conference on Advanced Information Science and System*, Association for Computing Machinery, New York, NY, USA, AISS '21, doi:10.1145/3503047.3503072, URL https://doi.org/10.1145/3503047.3503072.

WirelessWorld, R., 2012: Analog beamforming vs digital beamforming — difference between analog beamforming and digital beamforming. URL https://www.rfwireless-world.com/Terminology/Analog-Beamforming-vs-Digital-Beamforming.html, URL https://www.rfwireless-world.com/Terminology/Analog-Beamforming-vs-Digital-Beamforming.html.

Wolfley, O., D. Schvartzman, B. Mansur, J. Fusselman, R. Zhang, and B. Snelling, 2022: Three-dimensional anti-jamming array processing for gnss-based navigational aid inspection. 16, doi:10.1117/12.2618524.

Appendix A - List Of Symbols

$\mathbf{a}$	Antenna radiation pattern in form of azimuth response vector
$\hat{\boldsymbol{\theta}}$	θ unit vector
$\hat{\boldsymbol{\phi}}$	ϕ unit vector
$\vec{E}_{\hat{\boldsymbol{\theta}}}$	θ component of the electric field
$\vec{E}_{\hat{\boldsymbol{\phi}}}$	ϕ component of the electric field
j	Imaginary number equal to $\sqrt{-1}$
$\boldsymbol{\theta}$	θ phase shift in radians
$\boldsymbol{\phi}$	ϕ phase shift in radians
$E_{\boldsymbol{\theta}}$	Magnitude of the electric field in units of (V/m)
$E_{\boldsymbol{\phi}}$	Magnitude of the electric field in units of (V/m)
$\overline{E}$	Electric field of antenna
$\overline{E}_o$	Embedded element pattern
AF	Array Factor
N	Number of elements along the x-axis
n	The nth element along the x-axis
M	Number of elements along the y-axis
m	The mth element along the m-axis
k	The wave number equal to $\frac{2\pi}{\lambda}$
λ	The wavelength of the propagating signal
d	The distance between elements of a linear array
β_x	Phase component along the x-axis

β_y	Phase component along the y-axis
β	Total phase component combining β_x and β_y
G	Gain of antenna
$\mathbf{\Gamma}$	Active reflection co-efficient
ϵ_t	Total efficiency of the array
θ_o	Steering angle along the elevation plane
ϕ_o	Steering angle along the azimuth plane
θ	Observation angle along the elevation plane
ϕ	Observation angle along the azimuth plane
$\overline{E}_{max}$	The maximum of the electric field
D	Directvity of the array
d_x	Distance between elements along the x-axis of a planar array
d_y	Distance between elements along the y-axis of a planar array
$\mathbf{w}_{mn}$	Complex weight which is the steering vector for individual elements in a planar array.
a_{mn}	Amplitude excitation co-efficient for individual elements in a planar array.
$\odot$	This symbol denotes element-wise multiplication
w_o	Steering vector for signal of interest (SOI)
w_x	Steering vector for signal not of interest (SNOI)
w_o'	Complex conjugate transpose of w_o
w_x'	Complex conjugate transpose of w_x
r	Response of the SOI at the SNOI location
$\mathbf{W}$	Null-forming weight
$\overline{x}$	mean in dataset x
x_i	observation in dataset x
$\overline{y}$	mean in dataset y
y_i	observation in dataset y

n	number of values in dataset
$\mathbf{R}$	Covariance matrix of noise and signals not of interest (SNOI)
$\mathbf{R^T}$	Transpose of the covariance matrix
$\mathbf{E}$	Radiation pattern of individual elements
$\mathbf{Y}$	Total weighted sum of all element voltages
$Var(x)$	Variance within x dataset
$Cov(x, y)$	Covariance between x and y datasets

Appendix B - List Of Acronyms and Abbreviations

ARRC	Advanced Radar Research Center
AWG	Arbitrary Waveform Generator
ADC	Analog to Digital Conversion
BAE	British Aerospace Systems
COTS	Commercial Off-The-Shelf
MPAR	Multifunction Phased Array Radar
Dual-Pol	Dual Polarization
OU	University of Oklahoma
ECE	Electrical and Computer Engineering
PSL	Peak Sidelobe Level
cm	centi-meter
SBAS	Satellite Based Augmentation System
SLL	Sidelobe Level
SOI	Signal of Interest
SNOI	Signal Not of Interest
VNA	Vector Network Analyzer
SIR	Signal-to-Interference Ratio
SMA	SubMiniature version A Connector
FPGA	Field Programmable Gate Array
SNR	Signal-to-Noise Ratio
Tx	Transmit
Rx	Receive

RNSS	Regional Navigational Satelite System
dB	Decibel
GPS	Global Positioning System
GHz	Giga-Hertz
GNSS	Global Navigation Satellite System
ULA	Uniform Linear Array
BF	Beam-forming
RFI	Radio Frequency Interference
RF	Radio Frequency
FI	Flight Inspection
RHCP	Right Hand Circular Polarization
LHCP	Left Hand Circular Polarization
RNSS	Regional Navigation Satellite System
GBAS	Ground Based Navigational System
FAA	Federal Aerospace Administration
MS	Micro-strip
EM	Electromagnetic
PAC	Phased Array Controller
GUI	Graphical User Interface
AF	Array Factor
FF	Far-field
NF	Near-field
V-Pol	Vertical Polarization
H-Pol	Horizontal Polarization
km	kilo-meter
VHF	Very High Frequency
1D	One-Dimensional

2D	Two-Dimensional
3D	Three-Dimensional